SCIENCES

Geography and Demography, Field Director – Denise Pumain

Physical Geography, Construction of Environments and Landscapes, Subject Head – Étienne Cossart

Spatial Impacts of Climate Change

Coordinated by
Denis Mercier

Color Section

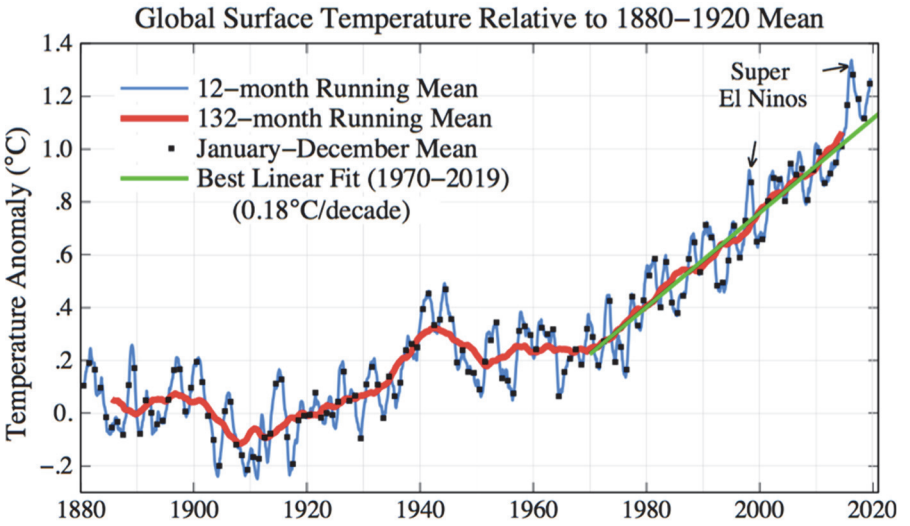

Figure 1.1. *Annual mean surface temperature from 1880 to 2019 compared to the 1880–1920 mean (source: Sato and Hansen, Climate Science, Awareness and Solutions at Columbia University Earth Institute, 2020)*

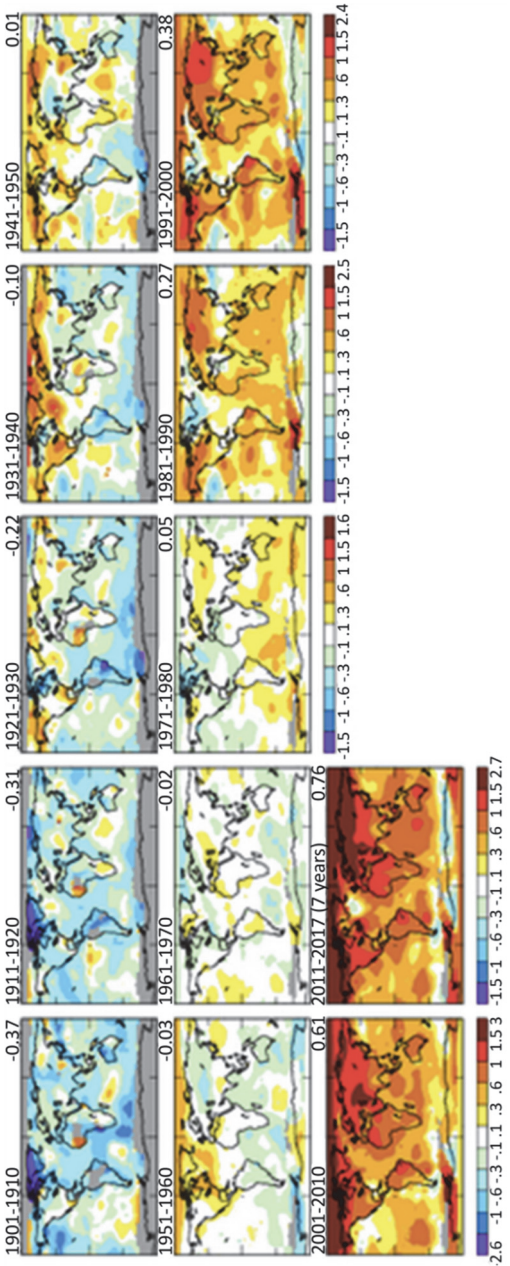

Figure 1.2. *Average surface temperature per decade from 1910 to 2017 compared to the 1951–1980 average (source: 2018 NASA-GISS temperature data, downloaded from https://data.giss.nasa.gov/gistemp/)*

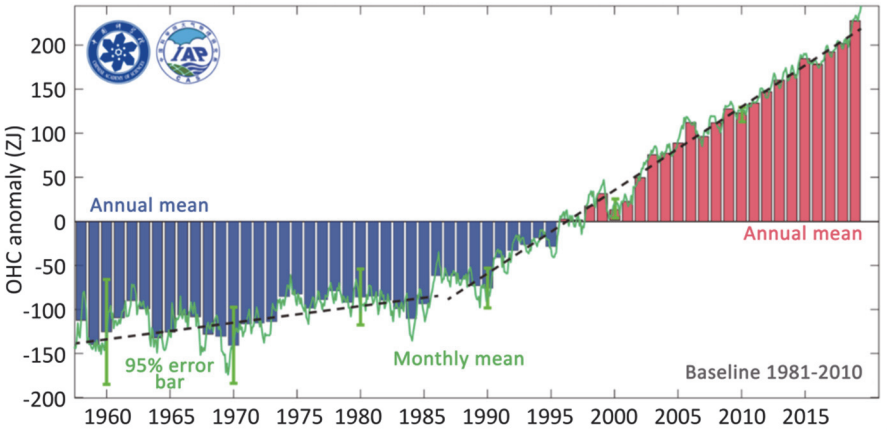

Figure 1.3. *Ocean heat content (OHC) in the upper water section above 2,000 m from 1955 to 2019*

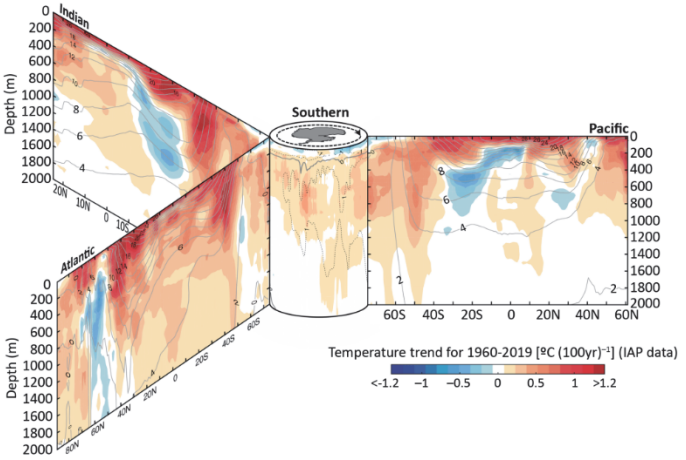

Figure 1.4. *Vertical cross-section of ocean temperature trends from 1960 to 2019 from the sea surface to 2,000 m (60-year ordinary least squares linear trend)*

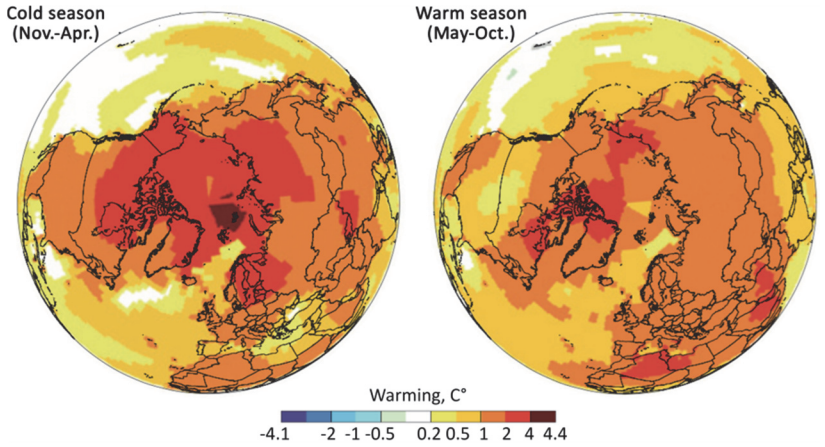

Figure 1.5. *Spatial distribution of Arctic warming for the period 1961–2014 for the cold season (November to April) and the warm season (May to October) (source: AMAP 2017)*

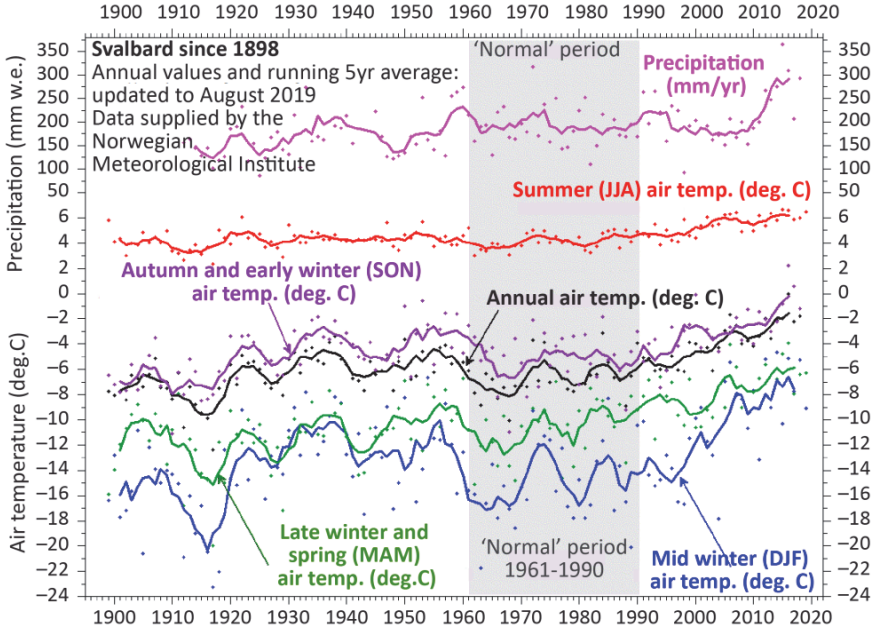

Figure 1.6. *Temporal distribution of air temperature warming at Longyearbyen, 78° 25' N, 15° 47' E, capital of the Svalbard archipelago, for the period 1898–2019 at different time scales, annual in black, summer (June, July, August) in red, autumn (September, October, November) in purple, winter (December, January, February) in blue, spring (March, April, May) in green*

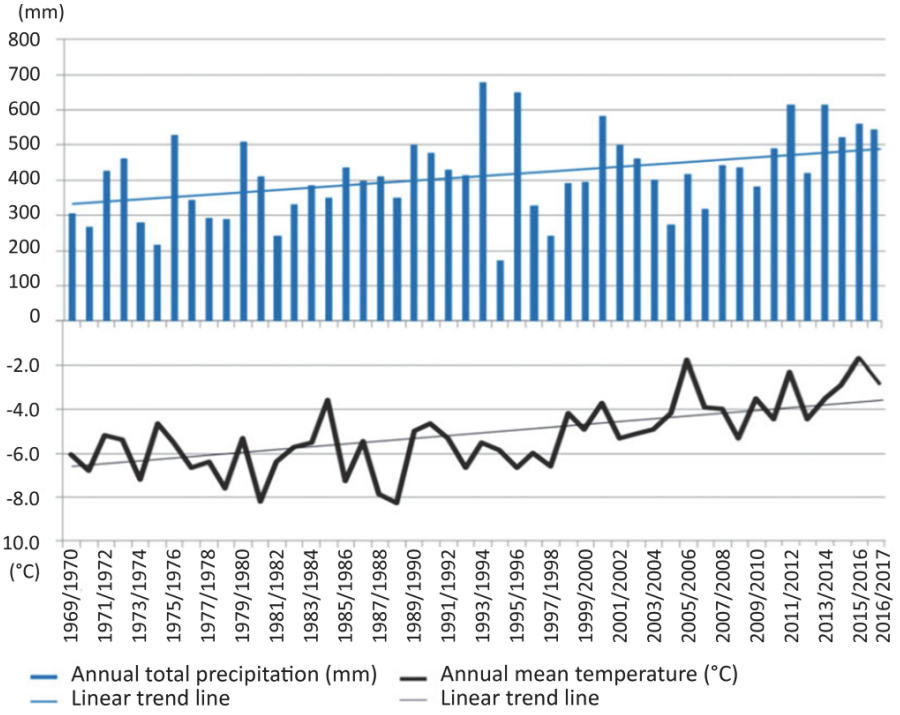

Figure 1.7. *Annual mean precipitation and annual mean temperatures from 1969 to 2016 at the Ny-Ålesund weather station (northwestern Spitsbergen, Svalbard) (source: Bourriquen et al. 2018, based on data from the Norwegian Meteorological Institute)*

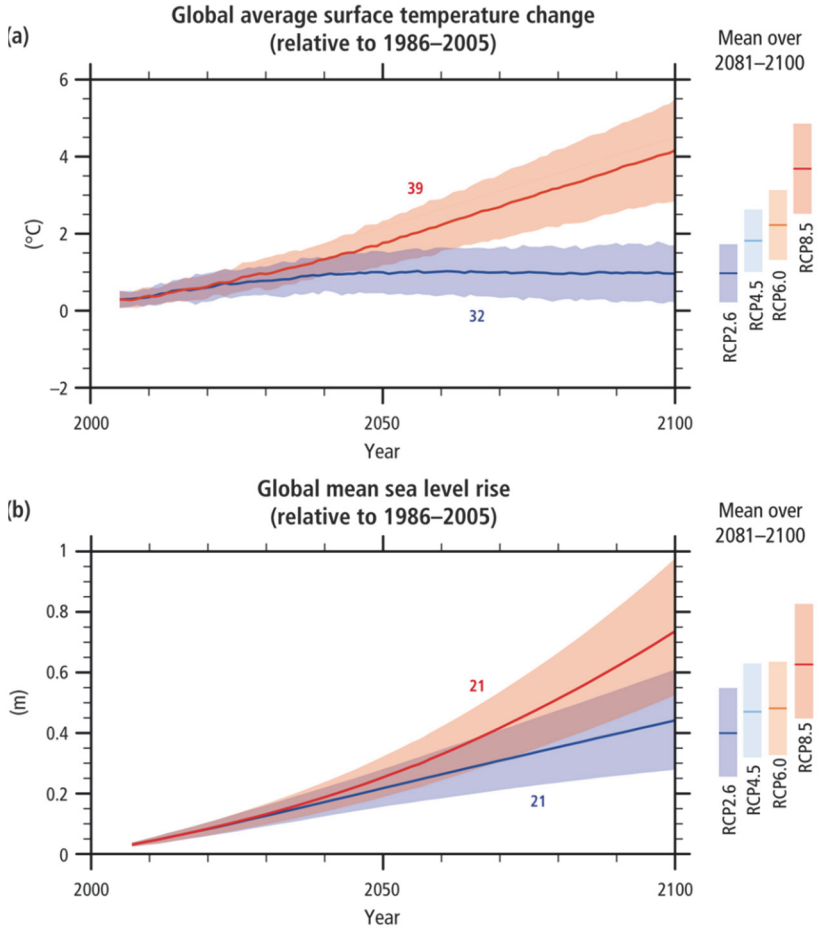

Figure 1.8. *(a) Mean change in surface temperature. (b) Mean sea-level rise from 2006 to 2100 (as determined by multi-model simulations).*

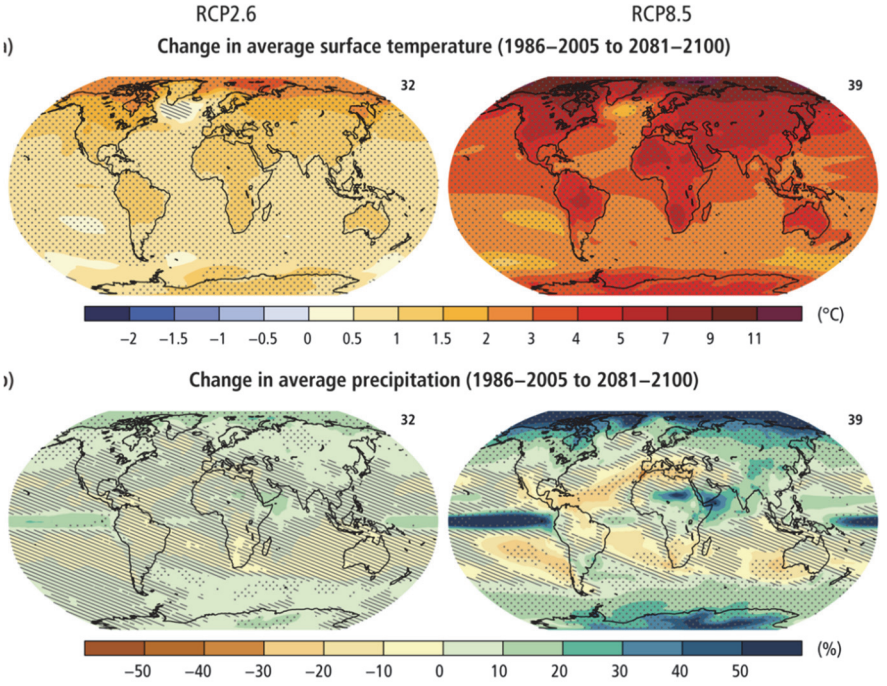

Figure 1.9. *(a) Change in mean surface temperature. (b) Change in mean precipitation based on the multi-model mean projections for 2081–2100 compared to 1986–2005 in the RCP2.6 (left) and RCP8.5 (right) scenarios.*

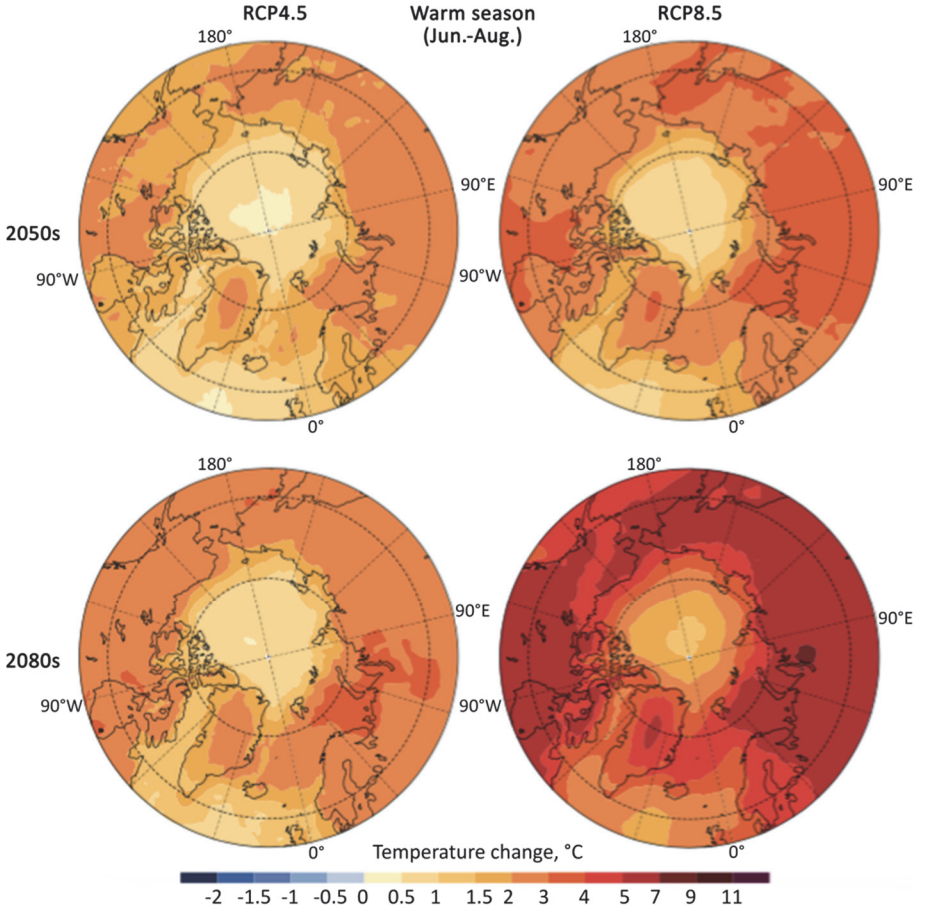

Figure 1.10. *Projected changes in summer surface temperatures (June to August) compared to the 1986–2005 average under scenario 4.5 and 8.5, for the years 2050 and 2080 (source: AMAP 2017)*

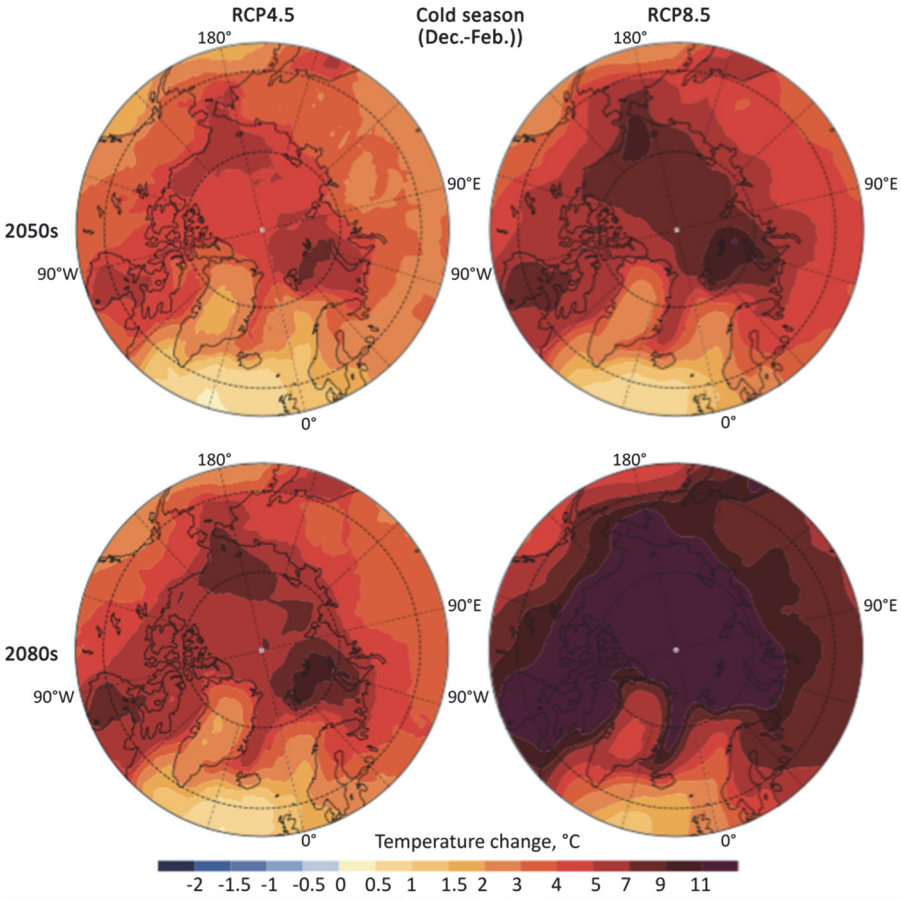

Figure 1.11. *Projected changes in winter (December to February) surface temperatures relative to the 1986–2005 average under scenarios 4.5 and 8.5, for the years 2050 and 2080 (source: AMAP 2017)*

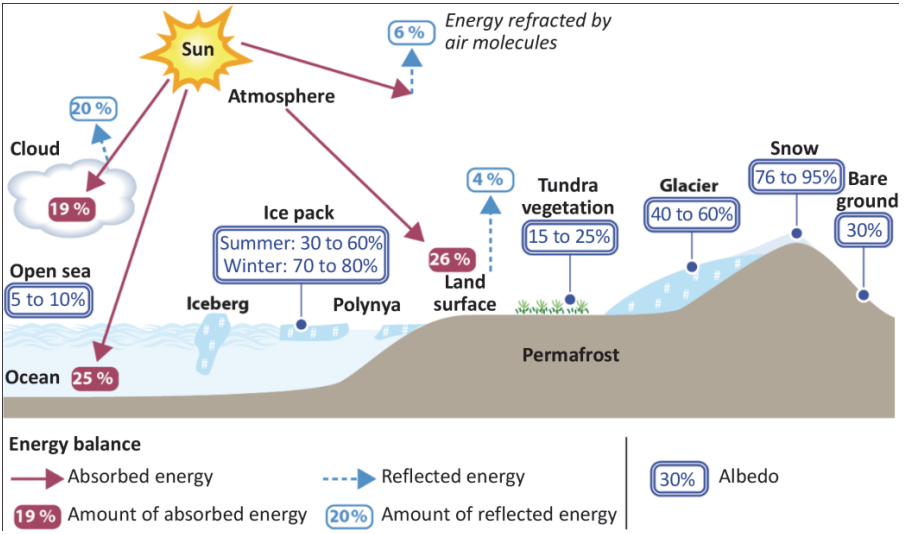

Figure 1.12. *Elements of the global energy balance and albedo of different surfaces in the Arctic (source: design D. Mercier, drawing by F. Bonnaud, Faculty of Arts, Sorbonne University, 2020)*

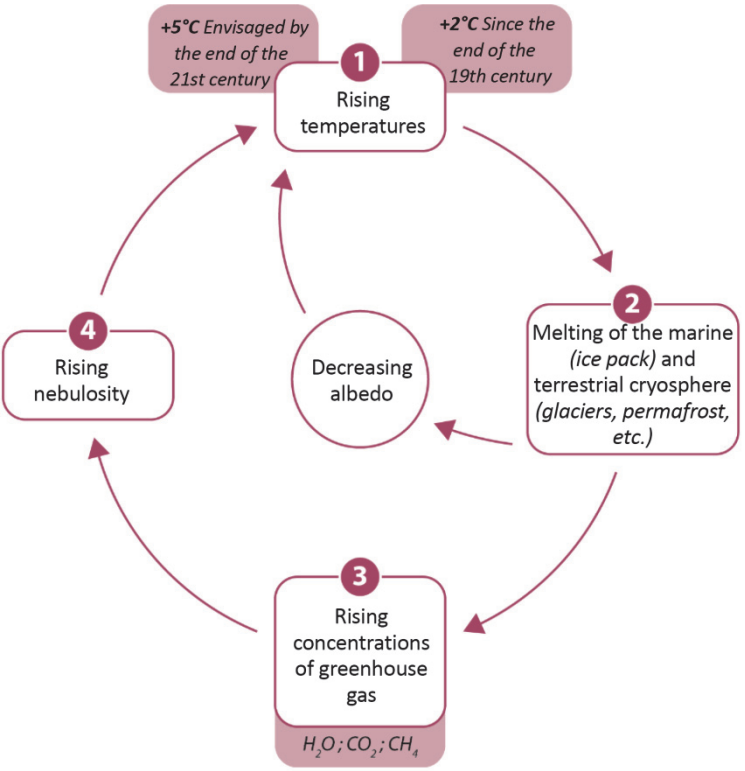

Figure 1.13. *Positive feedback loops explaining the amplification of Arctic climate warming (source: design D. Mercier, drawing by F. Bonnaud, Faculty of Arts, Sorbonne University, 2020)*

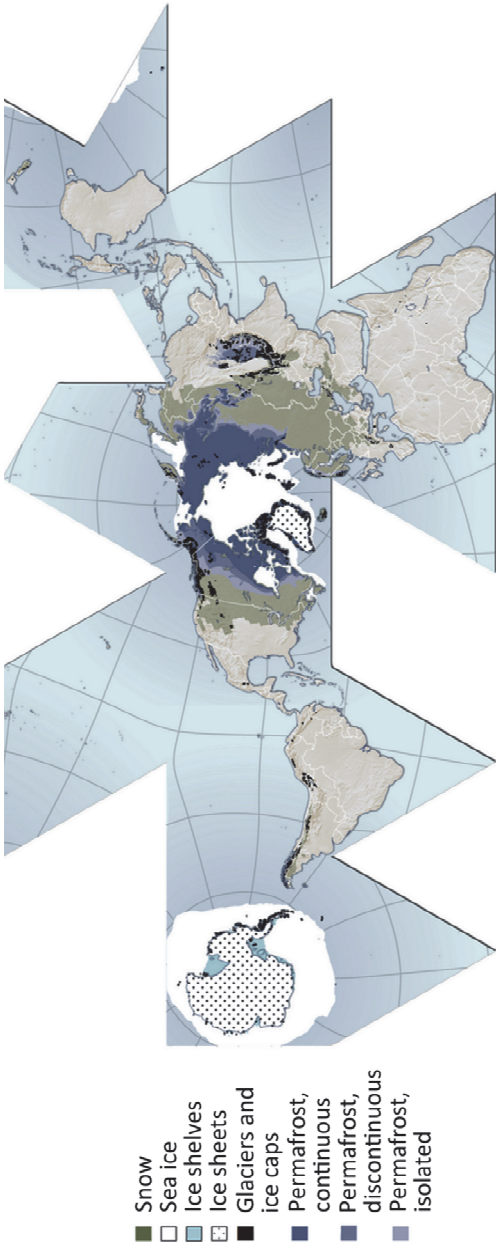

Figure 2.1. *Extension of the cryosphere (source: © Hugo Ahlenius, UNEP/GRID-Arendal)*

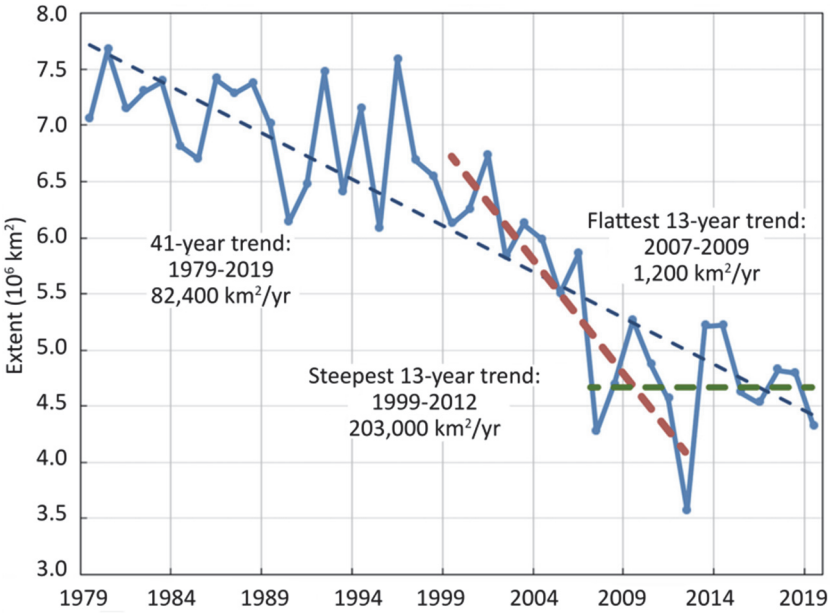

Figure 2.2. *Average Arctic sea ice extent for the month of September between 1979 and 2019. Decade of decline of 12.9%. (source: National Snow and Ice Data Center)*

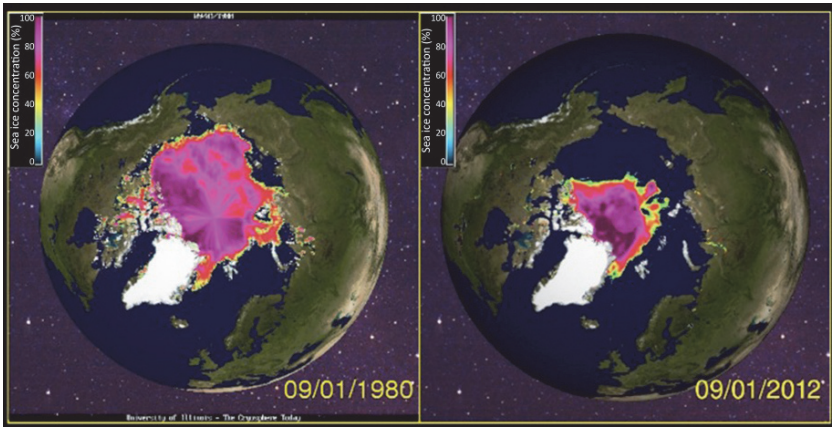

Figure 2.3. *Spatial extent of Arctic sea ice as of September 1, 1980, and on September 1, 2012, the year in which the extension was the least in the last four decades (source: The Cryosphere Today)*

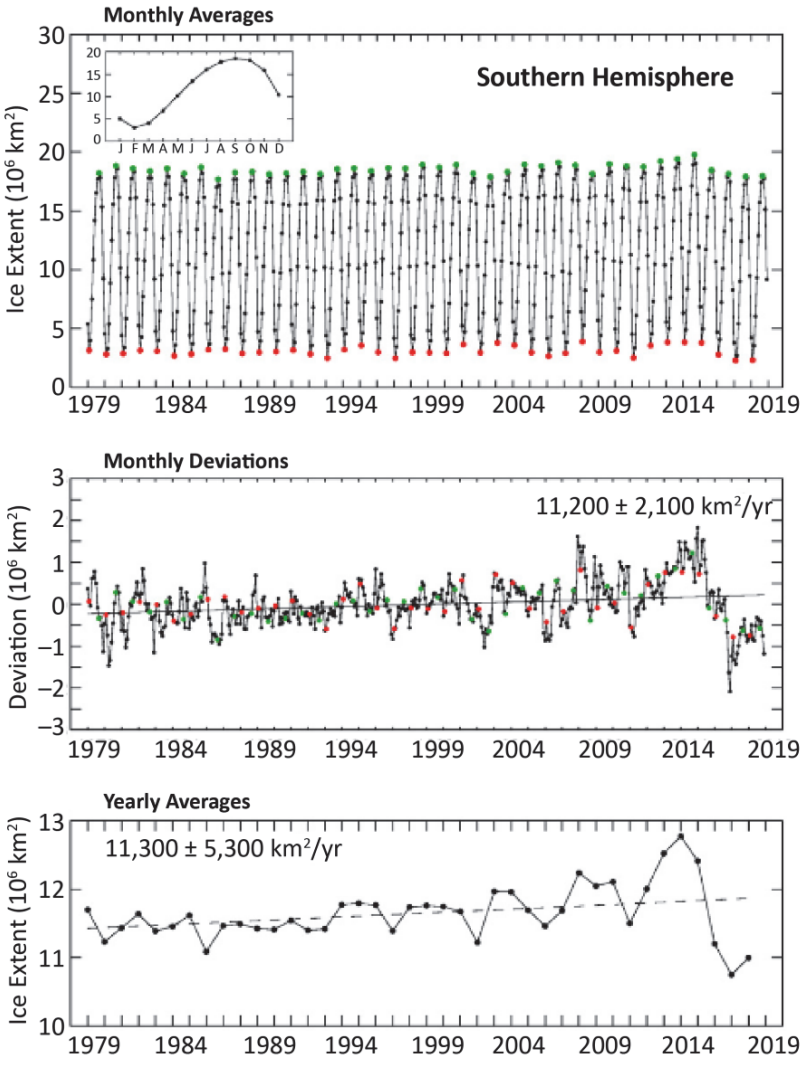

Figure 2.5. *Antarctic sea ice extents derived from satellite data DMSP Nimbus7 and NASA (source: Parkinson 2019)*

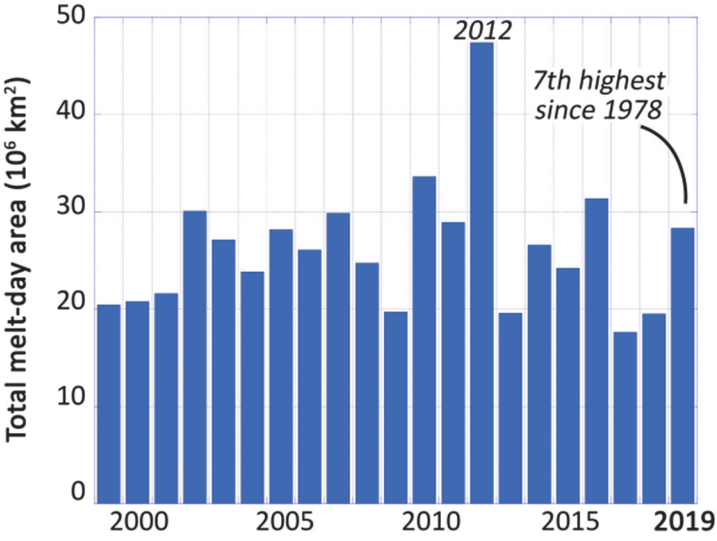

Figure 2.6. *Total extent of melt day, or sum of daily melt area during the 1999–2019 melt season in Greenland (source: NSIDC)*

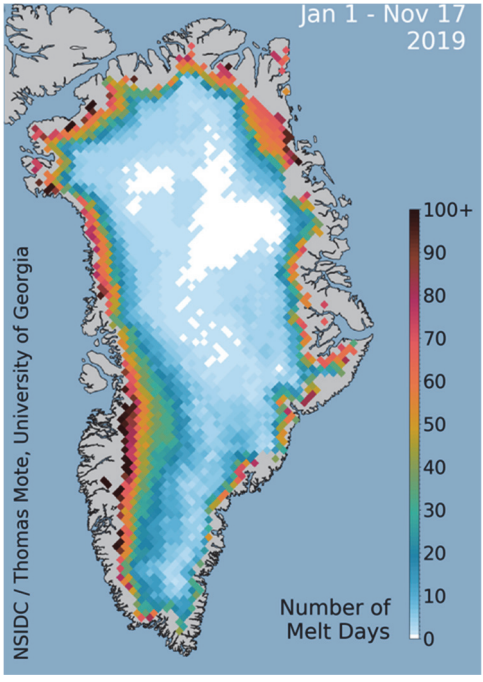

Figure 2.7. *Number of days of melt at the surface of Greenland's ice sheet between January 1 and November 17, 2019 (source: NSIDC, Thomas Mote, University of Georgia)*

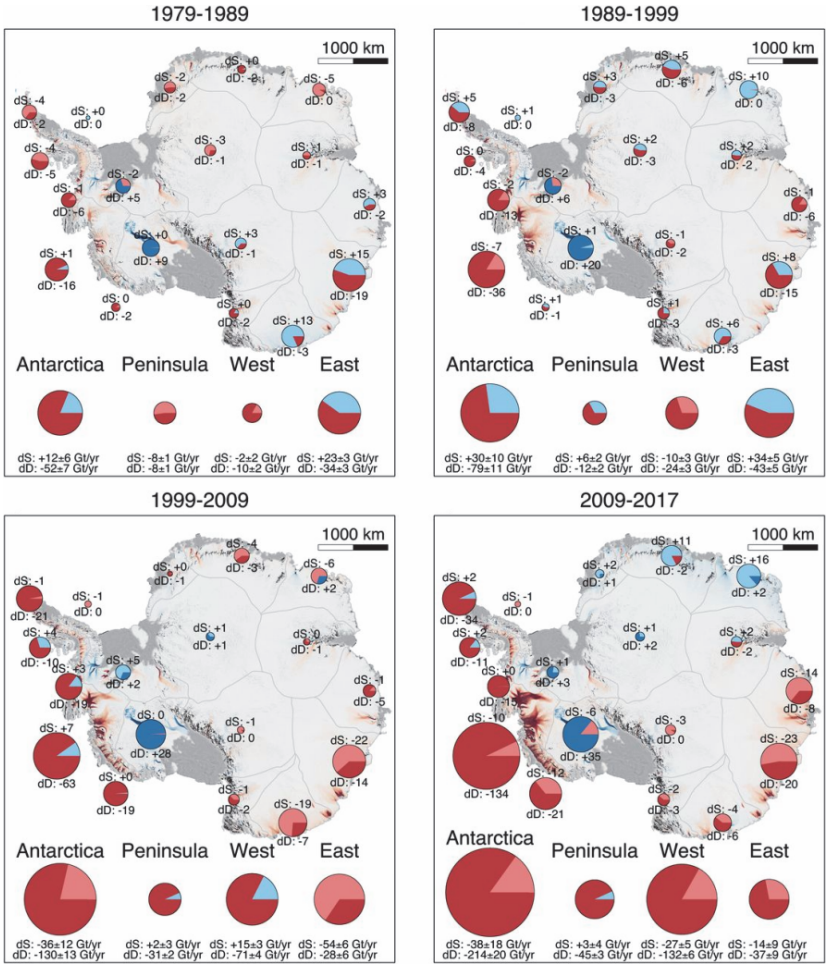

Figure 2.8. *Mass balance of the Antarctic ice sheet*

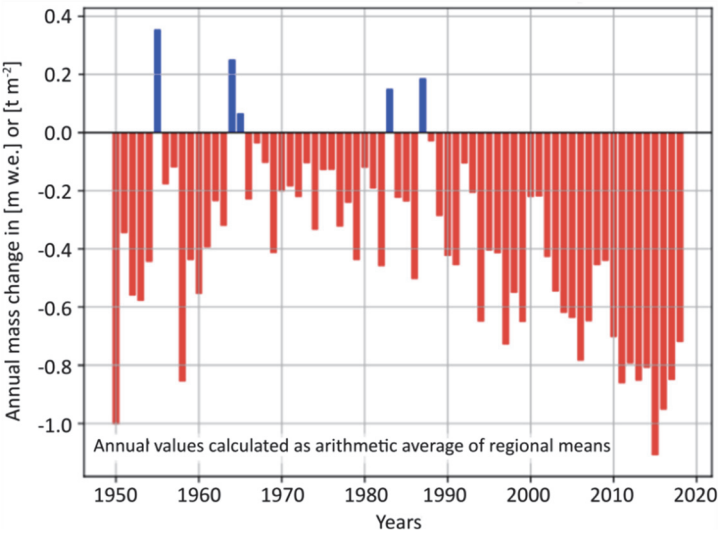

Figure 2.9. *Annual mass balance of reference glaciers with more than 30 years of glaciological measurements from 1950 to 2018. The values of annual mass change are given on the y-axis in water equivalent (w.e.) per meter of water, which corresponds to tons per square meter (t/m^2) (source: Zemp* et al. *2017).*

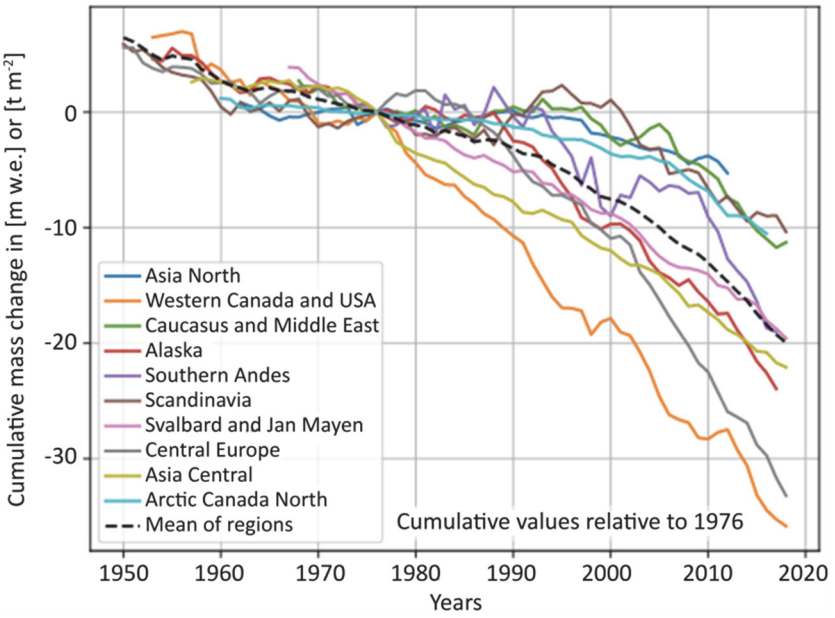

Figure 2.10. *Cumulative mass change from 1976 for regional and global averages based on reference glacier data (source: Zemp et al. 2017)*

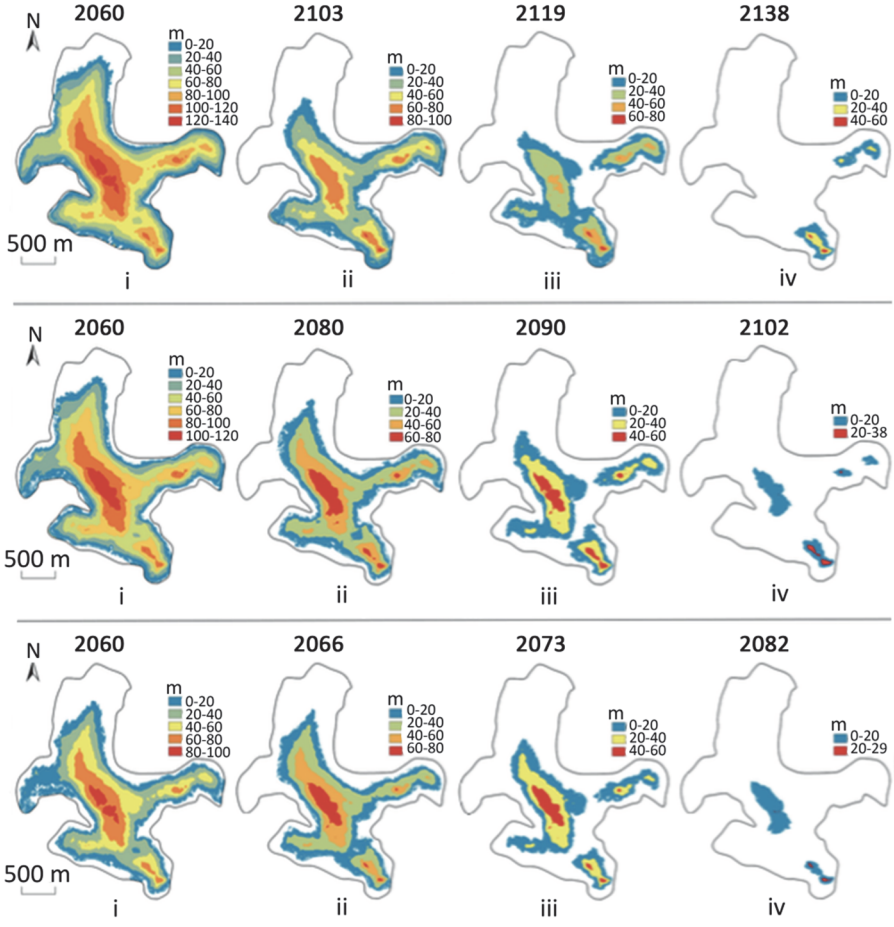

Figure 2.11. *Area and thickness of the Austre Lovénbreen glacier (Svalbard) simulated for different years: (i) 50th year (2060); (ii) disappearance of the western tributary; (iii) break between the main current and the eastern tributary; (iv) late decomposition according to the scenarios (a) optimistic; (b) high probability; (c) pessimistic (source: Wang* et al. *2019).*

Figure 2.12. *The Austre Lovénbreen glacier in northwestern Spitsbergen (Svalbard) in the background. The flat space in front of the glacier corresponds to the space freed by its melting since the beginning of the 20th Century. In the foreground, the prograding deltas on the Kongsfjorden are fed with sediments by the meltwater runoff from the glacier (source: © photo by D. Mercier taken on August 24, 2017).*

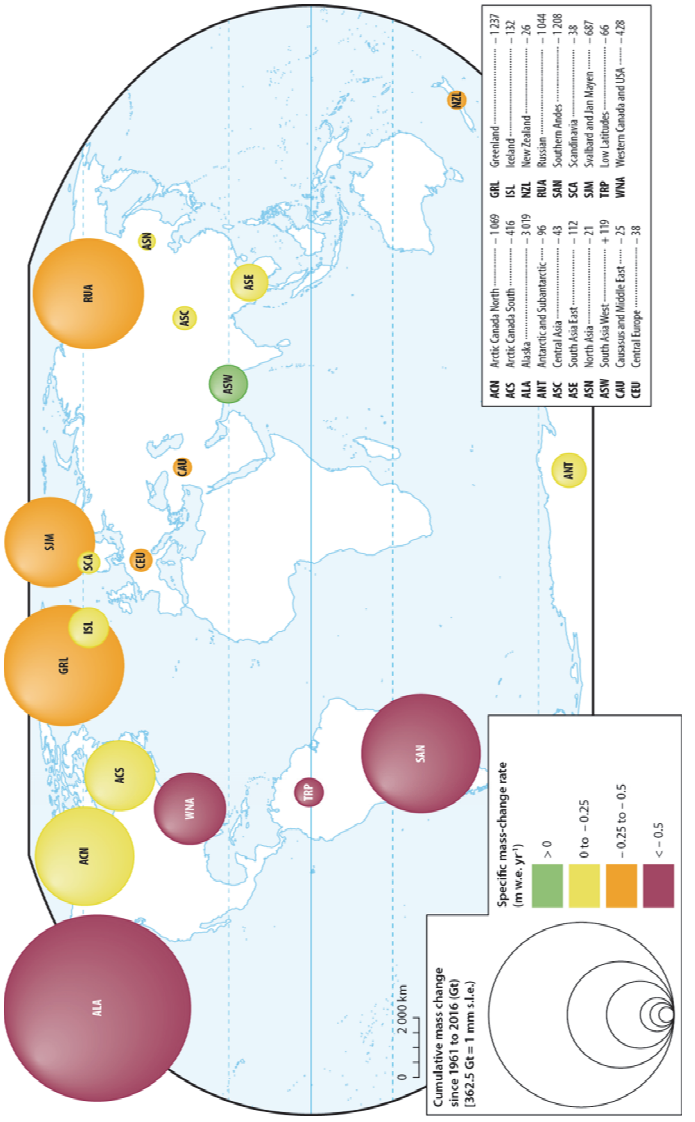

Figure 2.13. *Regional share of glaciers in sea-level rise from 1961 to 2016. The cumulative change in regional and global glacier mass (in gigatons, 1 Gt = 1,000,000,000 tons) corresponds to the size of the circles. The synthesis is based on 19,000 glaciers worldwide (source: modified from Zemp* et al. *2019)*

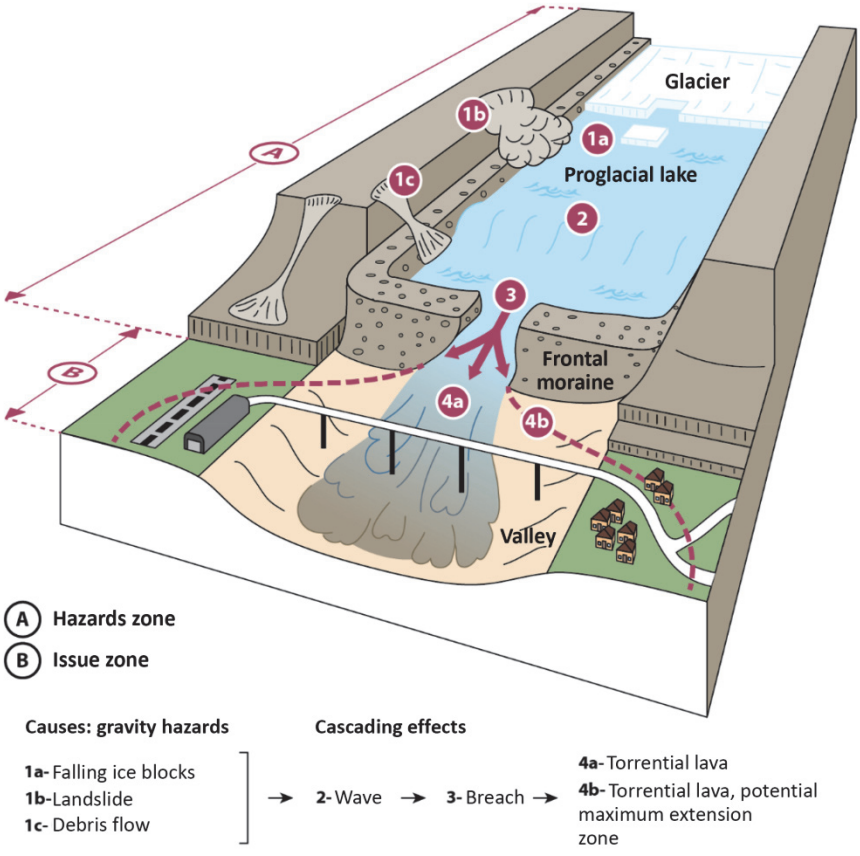

Figure 2.14. *Paraglacial hazards induced by melting glaciers (source: design D. Mercier; drawing F. Bonnaud, Sorbonne University, 2019)*

Figure 3.1. *The Arctic, a macro-region with variable spatialization, map proposed by the NORDREGIO Institute in 2015 (source: AHDR, AMAP and CAFF, analysis and design: J. Roto)*

Figure 3.2. *The political Arctic, nations and territories (source: Canobbio 2011)*

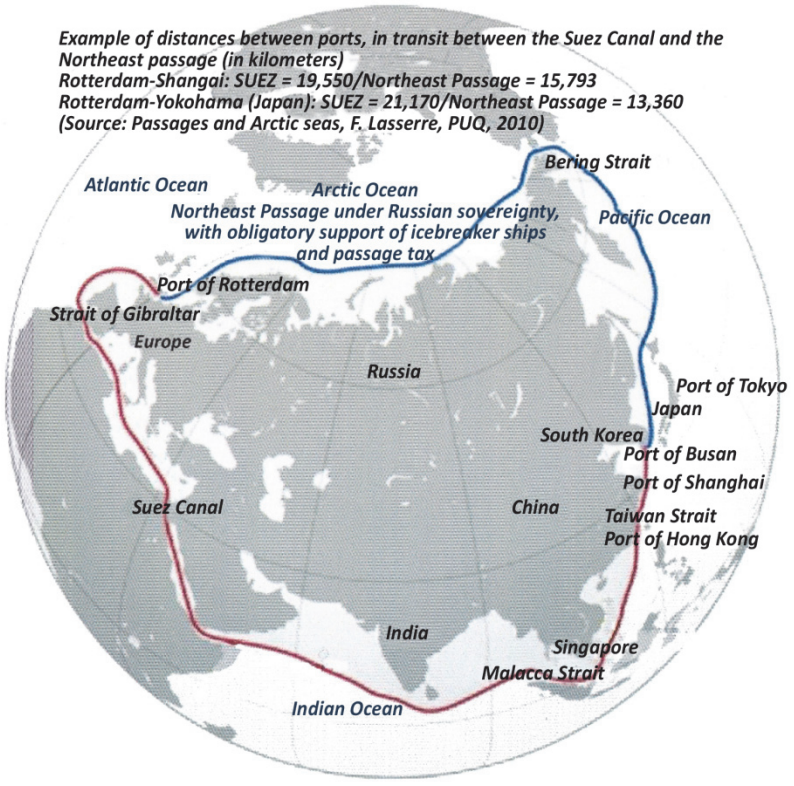

Figure 3.3. *A tenacious representation: Arctic integration through the routes of globalization (source: Canobbio 2019, based on a map by the Baltic shipowner Tschudi, in the 10th Annual Russian-Norwegian Oil and Gas Conference, Oslo, January 25, 2012)*

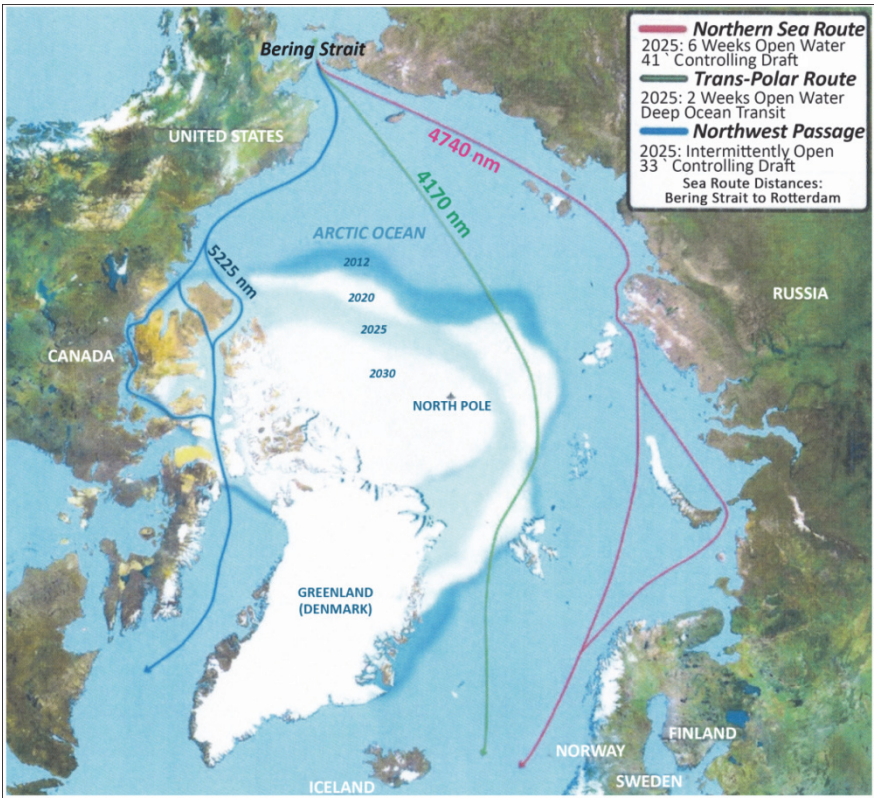

Figure 3.4. *Polar shipping routes (in nautical miles, nm) and the reduction of summer sea ice: mapping a new "transpolar route" incorporates the evolution of sea ice by 2030 (source: U.S. Navy 2014)*

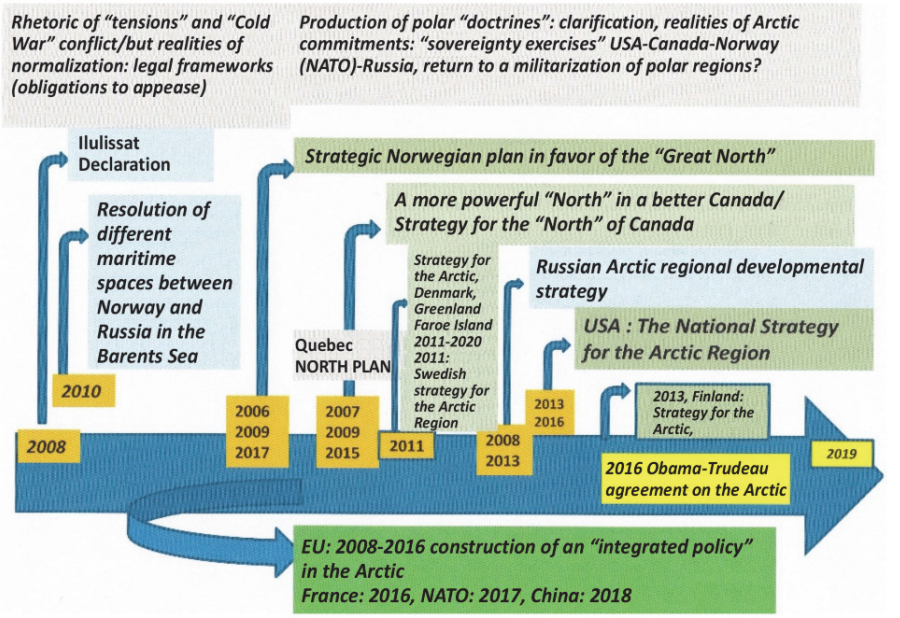

Figure 3.6. *Schematic representation of the production of Arctic policies during the period 2008–2018 (source: Canobbio 2019)*

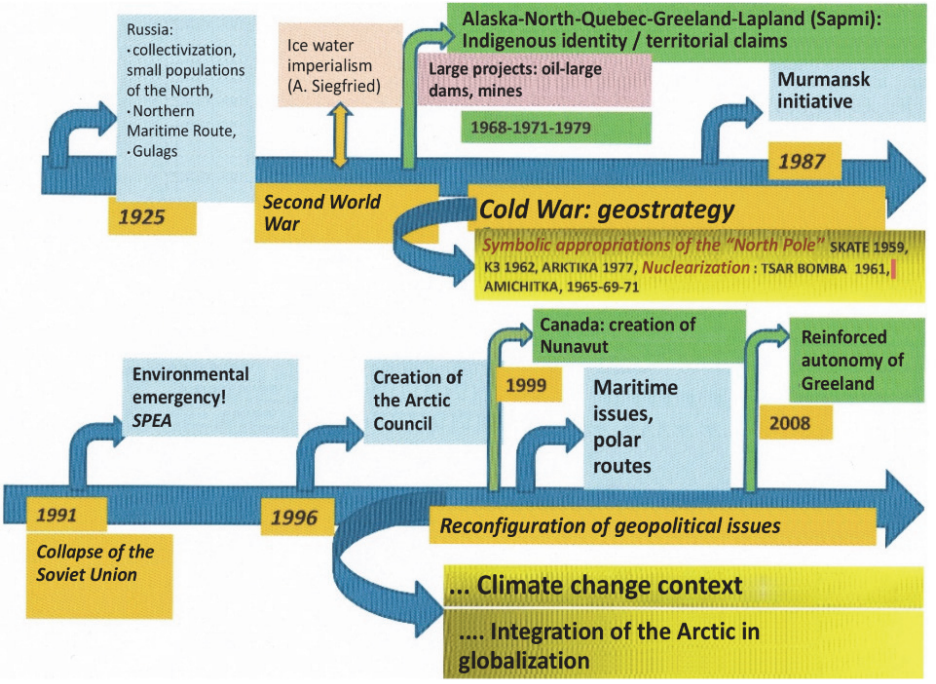

Figure 3.7. *Simplified schematic approach to historical trajectories of national recompositions and global contexts in the Arctic during the period 1925–2008 (source: Canobbio 2019)*

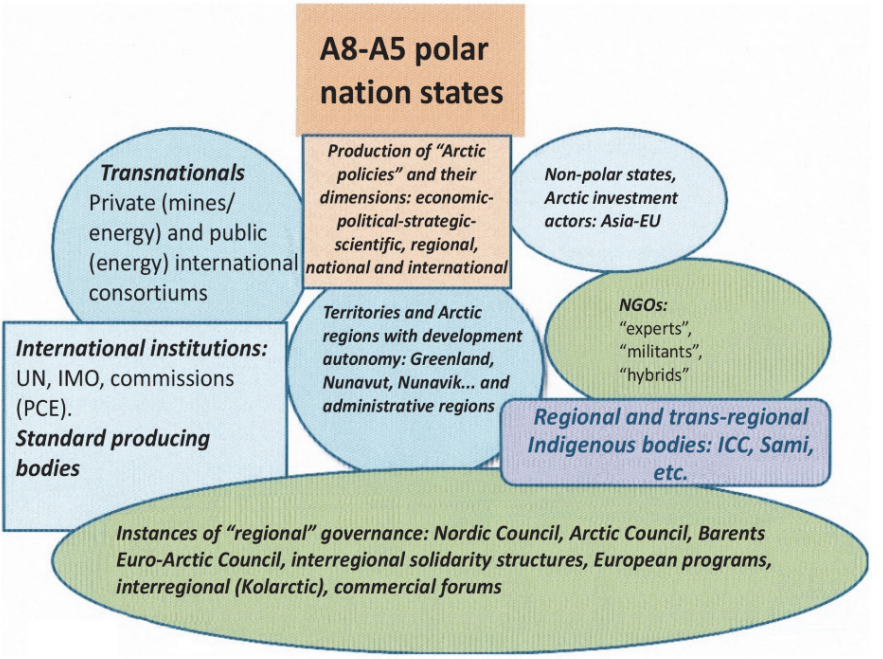

Figure 3.8. *Schematic representation of "stakeholder" actors in the Arctic (source: Canobbio 2019)*

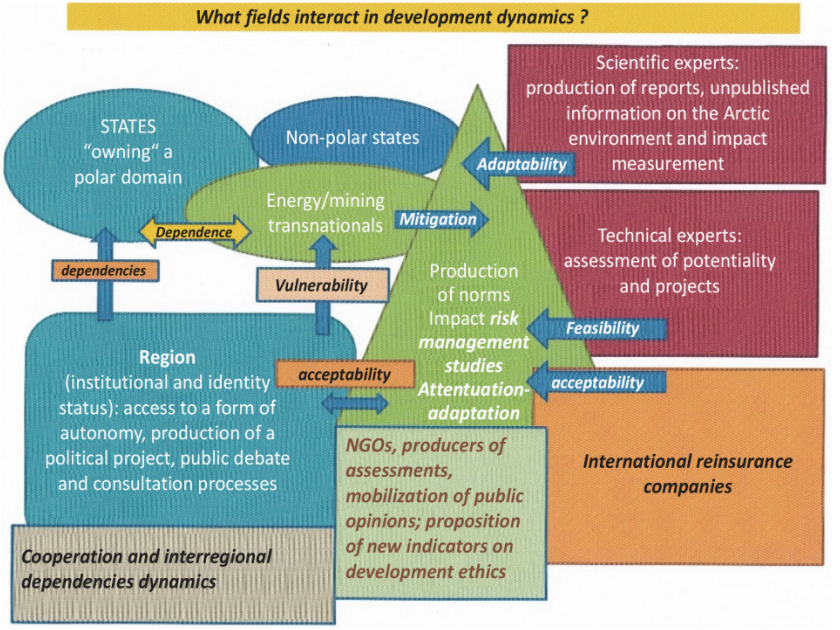

Figure 3.9. *The relational dynamics between "stakeholders" in northern-Arctic developments (source: Canobbio 2019)*

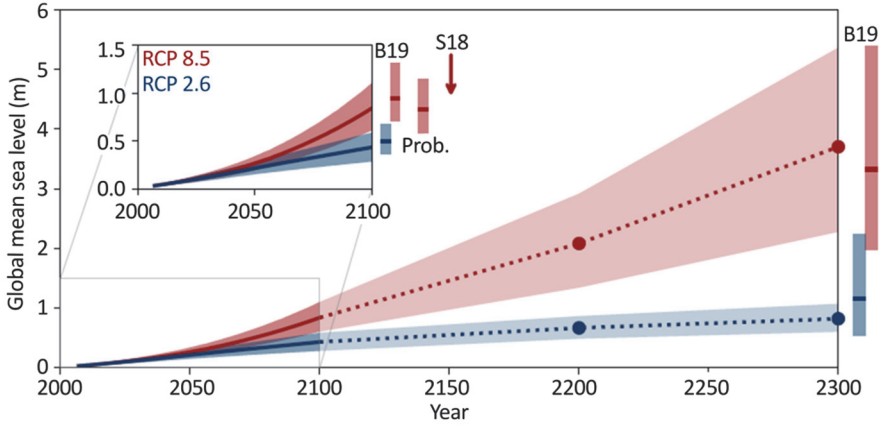

Figure 4.1. *Projections of sea-level rise between 2000 and 2300 for two greenhouse gas emission scenarios: RCP 2.6, "optimistic" scenario; RCP 8.5, "pessimistic" scenario (source: IPCC 2019)*

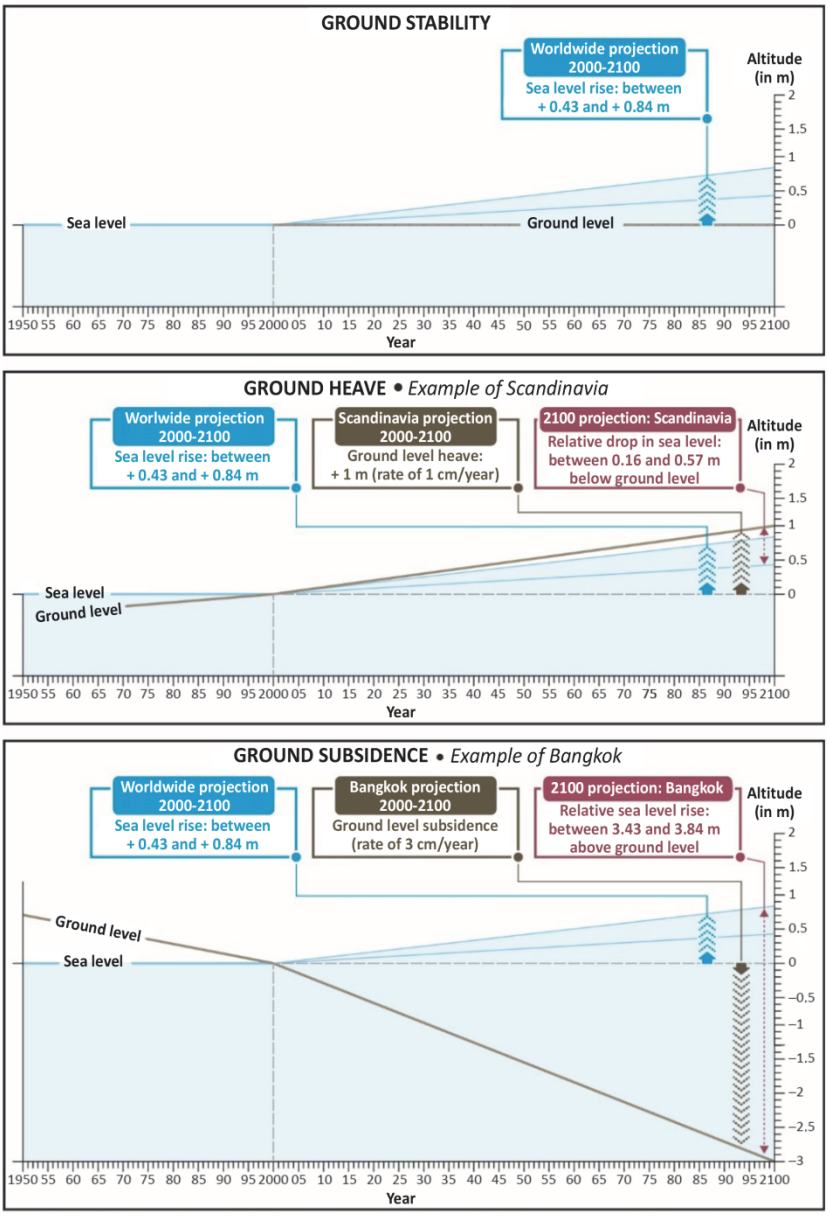

Figure 4.2. *The concept of relative sea level on coastlines as a function of different isostatic behaviors (source: adapted from Paskoff 2001)*

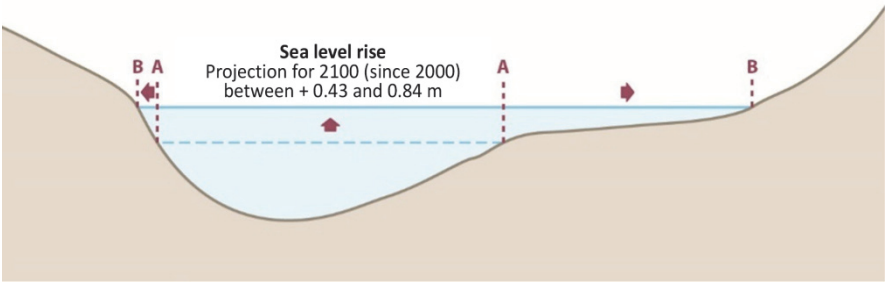

Figure 4.3. *Flooding processes associated with different types of coasts (source: adapted from Paskoff 2001)*

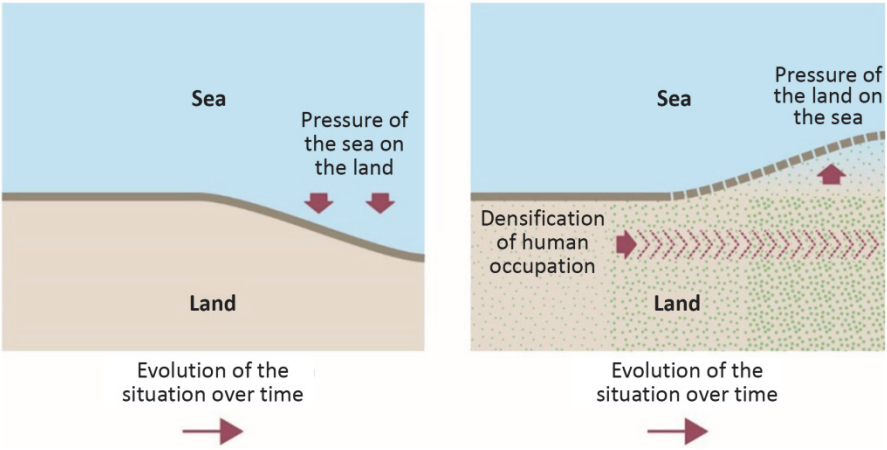

Figure 4.7. *Schematic illustration of the increase in coastal risks due to natural forcings exerting pressure from the sea to land (left) and anthropogenic forcings marked by a densification of populations and activities over time (green dots) and an overhang on the sea (right) (source: Creach 2020, adapted from Meur-Férec and Morel 2004)*

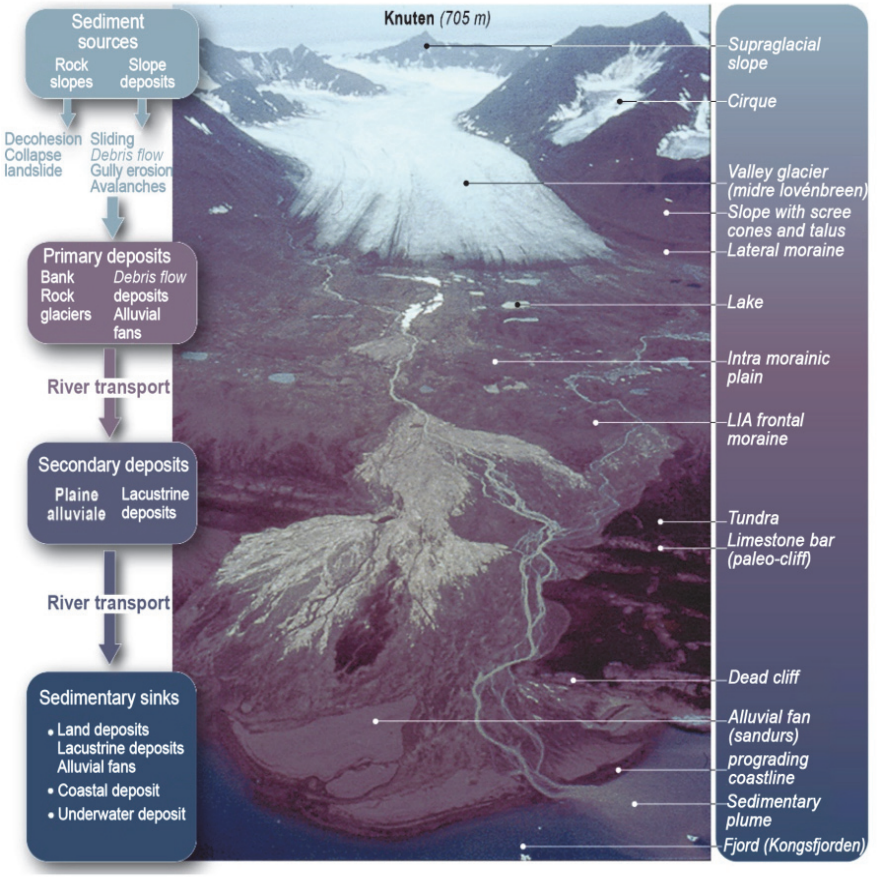

Figure 5.3. *Paraglacial sedimentary cascade for a small partially ice-covered polar watershed in northwestern Spitsbergen, Svalbard archipelago. The Midtre Lovénbreen glacier has been retreating since the beginning of the 20th Century as a result of contemporary climate warming in the Arctic (source: Mercier 2011).*

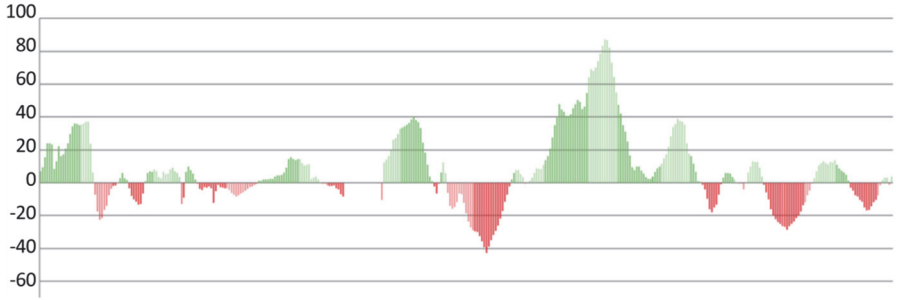

(a) Evolution of the coastline in meters from 1966 to 2017

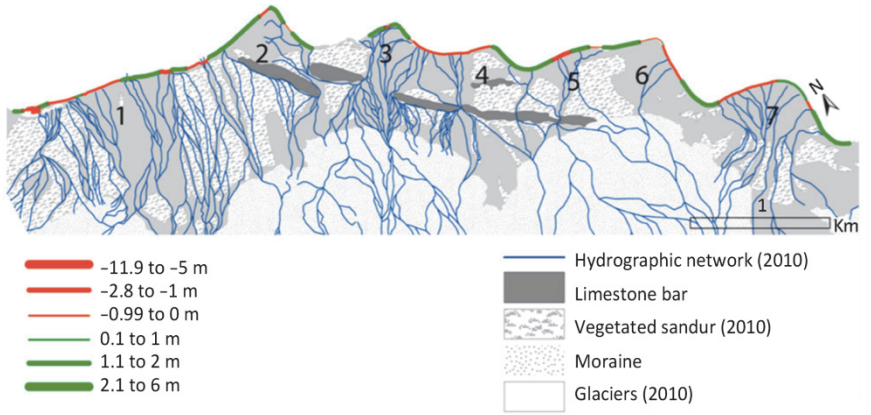

(b) Change in coastline in meters per year from 2016 to 2017

Figure 5.4. *Prograding and/or coastal erosion of the south bank of the Kongsfjorden in connection with the river system on the margins of the Loven glaciers in North-Western Spitsbergen (source: based on Bourriquen* et al. *2018)*

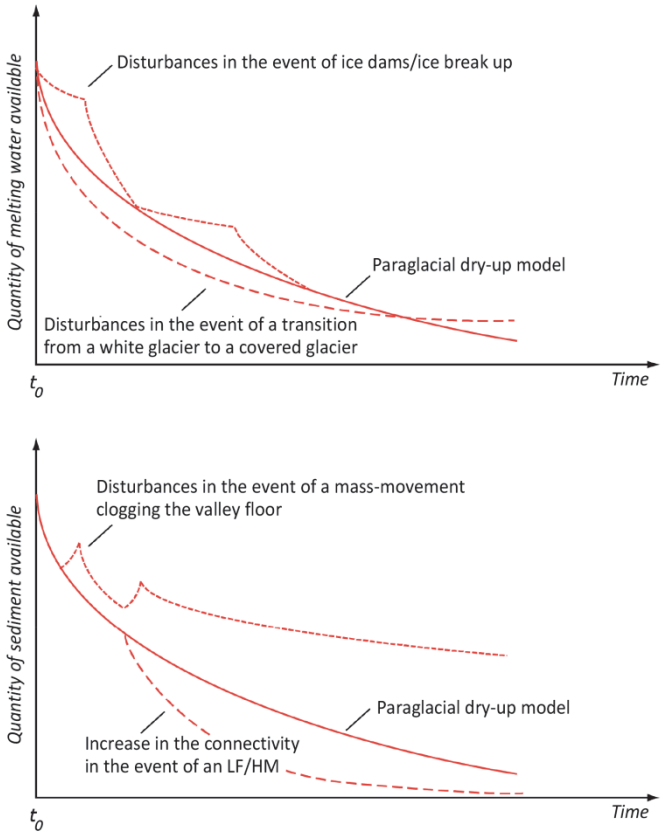

Figure 5.6. *Decoupled evolution of hydrological and sedimentary signals in a paraglacial context (source: modified from Knight and Harrison 2018)*

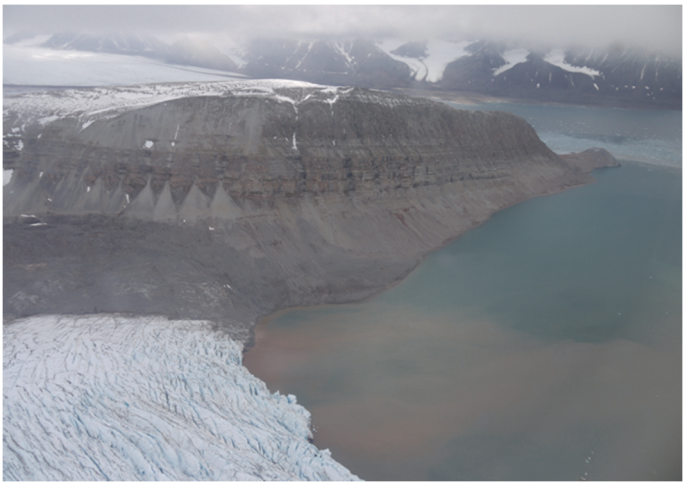

Figure 5.9. *The northern slope of the Colletthøgda Mountain in the inner part of the Kongsfjorden (78° 55' N, 12° 35' E)*

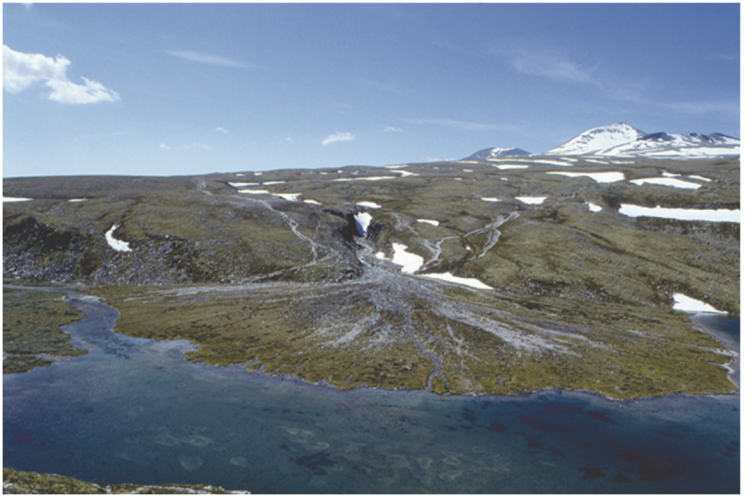

Figure 5.10. *Paraglacial Jutulhogget alluvial fans fed by the Kaldbekken stream at the outlet of the Kaldbekbotn valley in the Rondane massif in Norway (61° 53' N, 9° 47' E, 1,167 m above sea level)*

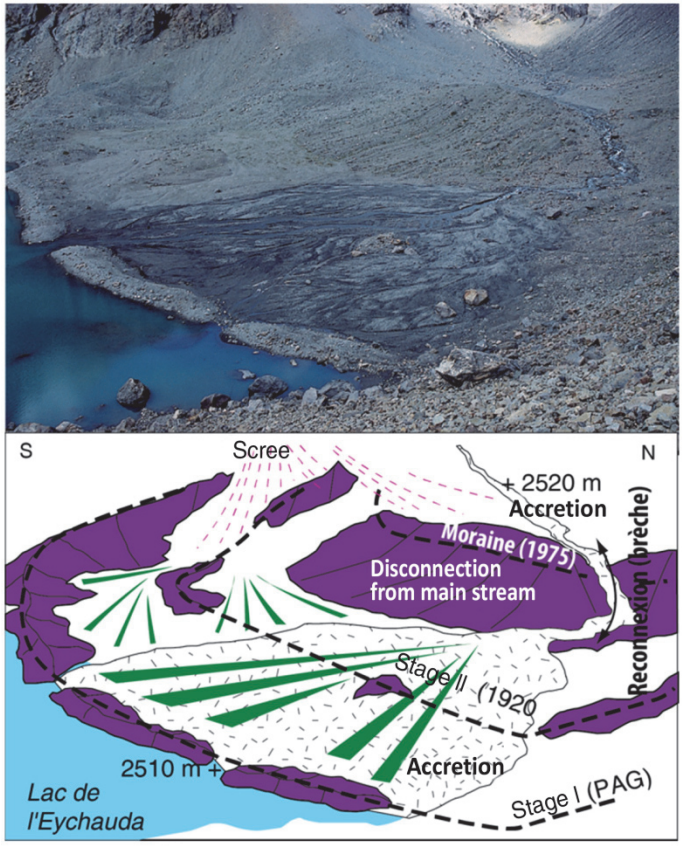

Figure 5.12. *Example of sedimentary filling on a margin undergoing post-LIA de-icing (Eychauda glacier, Hautes-Alpes, France, 2009)*

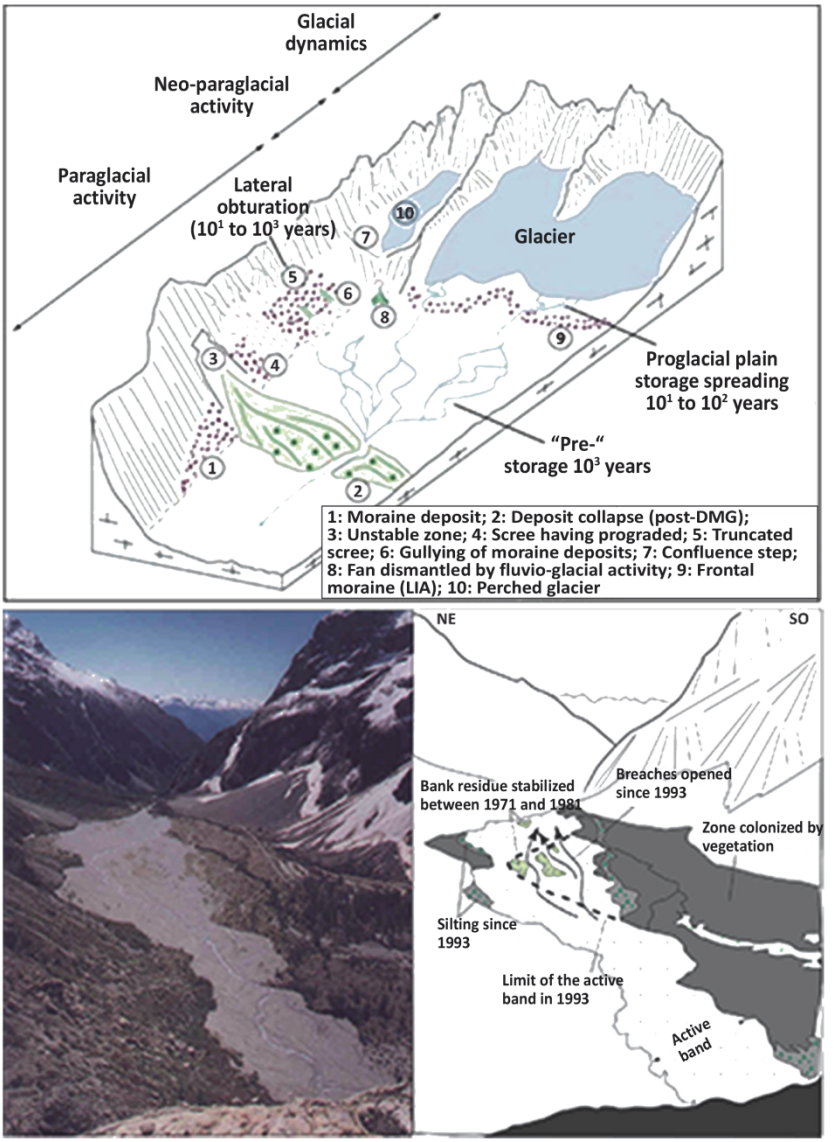

Figure 5.13. *Examples of sustainable storage phenomena in a paraglacial context. The mass movement deposits, like the Pré de Madame Carle deposit (Hautes-Alpes) (bottom), are effective dams that hinder sedimentary transfer on a millennial scale (source: design and construction, É. Cossart)*

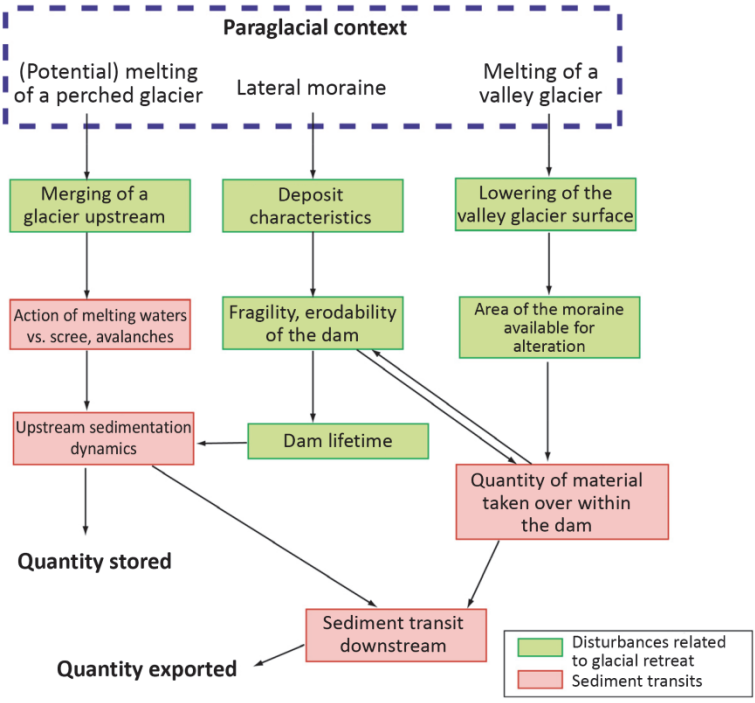

Figure 5.14. *Sedimentary budgets of upper watersheds affected by mass movements impeding sediment flow. The reservoir thus created causes an accretion from which sediment export remains very small in relation to the magnitude of the sedimentary volumes involved, brought by the slopes (source: modified from Cossart and Fort 2008b)*

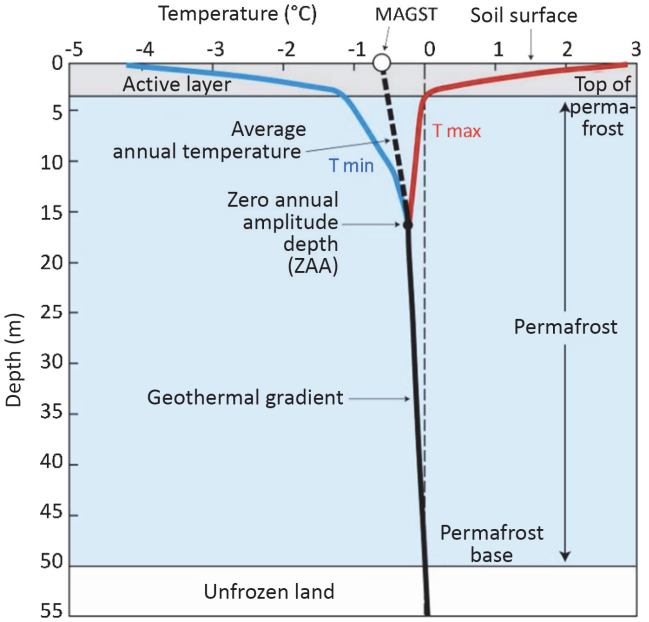

Figure 6.1. *Vertical profile of permafrost. The active layer (gray) thaws each summer and refreezes in winter when air temperatures become negative. The temperature of the permafrost (in blue) remains constantly ≤ 0°C. Dotted line represents the mean annual ground surface temperature (MAGST) (source: based on Ravanel 2010)*

Figure 6.2. *Maps of permafrost in both hemispheres (source: Brown* et al. *1997).*

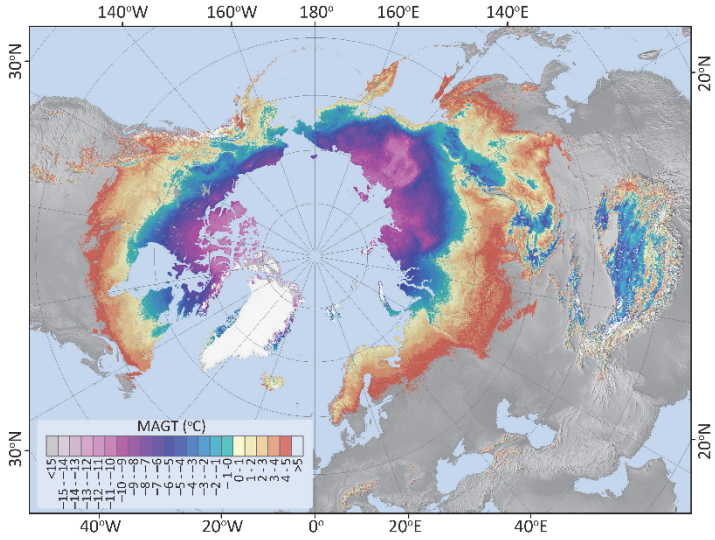

Figure 6.3. *Map of mean annual soil temperatures (2000–2016) in the Northern Hemisphere (source: Obu* et al. *2018)*

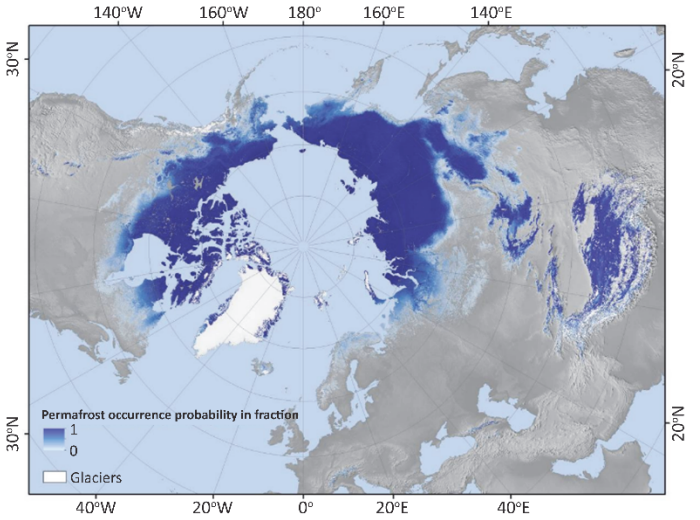

Figure 6.4. *Probability of occurrence of permafrost for the Northern Hemisphere derived from the mean annual ground temperature map (Figure 6.3) (source: Obu* et al. *2018)*

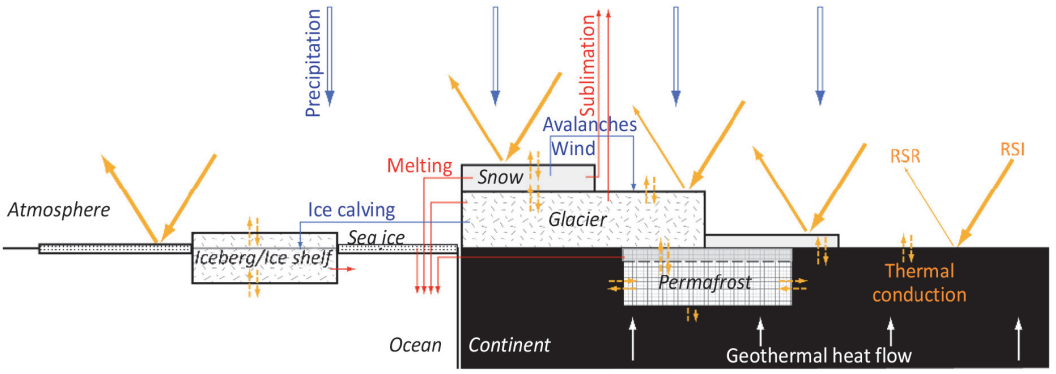

Figure 6.6. *All radiative exchanges affecting permafrost in a complex system within the cryosphere, driven by numerous feedbacks related to interactions with the ice field and snow cover in particular (source: based on Cossart 2014)*

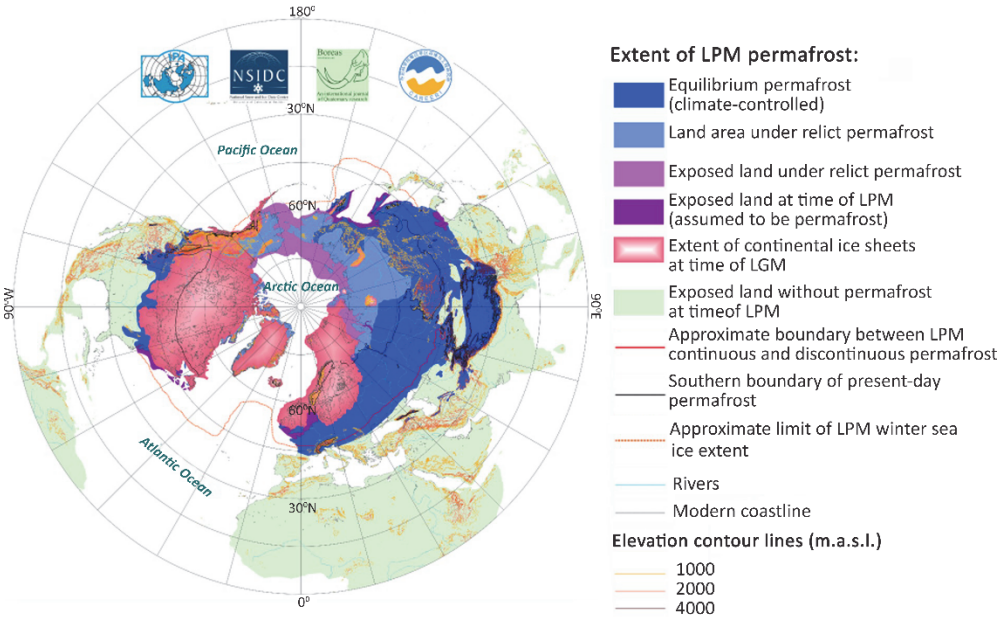

Figure 6.7. *Extension of permafrost during the Last Permafrost Maximum (LPM) in the Northern Hemisphere (source: Vandenbergh* et al. *2014)*

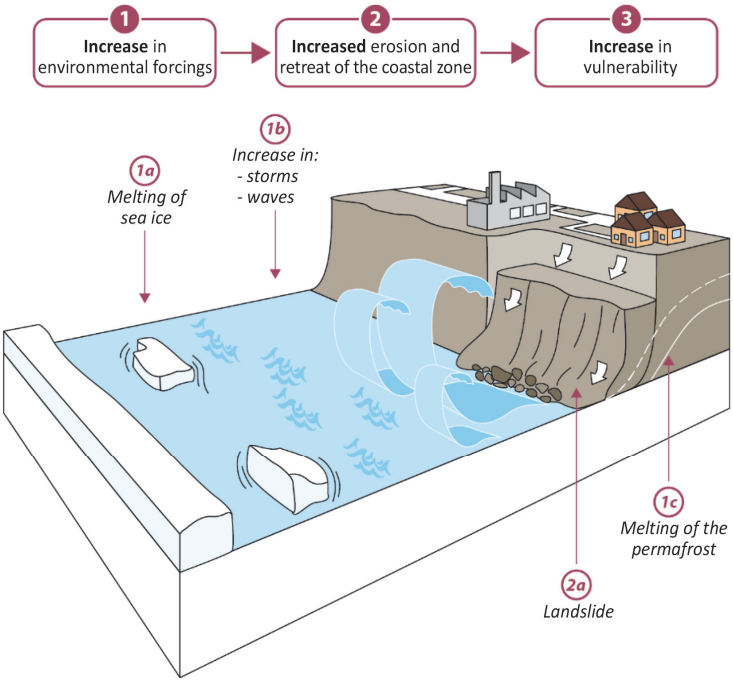

Figure 6.9. *Changing environmental forcing on the Arctic Basin coastlines and the implications for shoreline erosion and issues (source: design: D. Mercier; drawing: F. Bonnaud, Sorbonne University, 2019).*

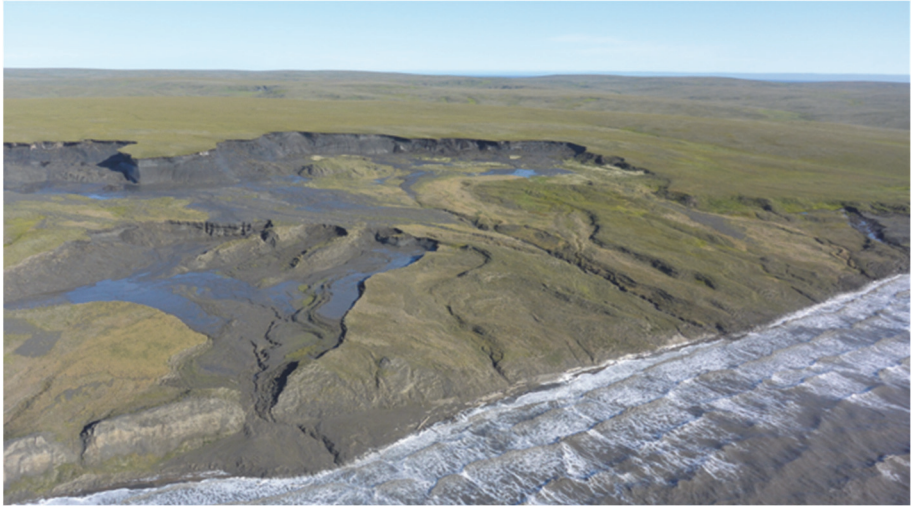

Figure 6.10. *Large active paraperiglacial landslides related to contemporary melting of permafrost on Herschel Island, Canada, on the southern shore of the Beaufort Sea (69° 36' N, 139° 04' W) (source: Alfred Wegener Institute, Potsdam, Germany)*

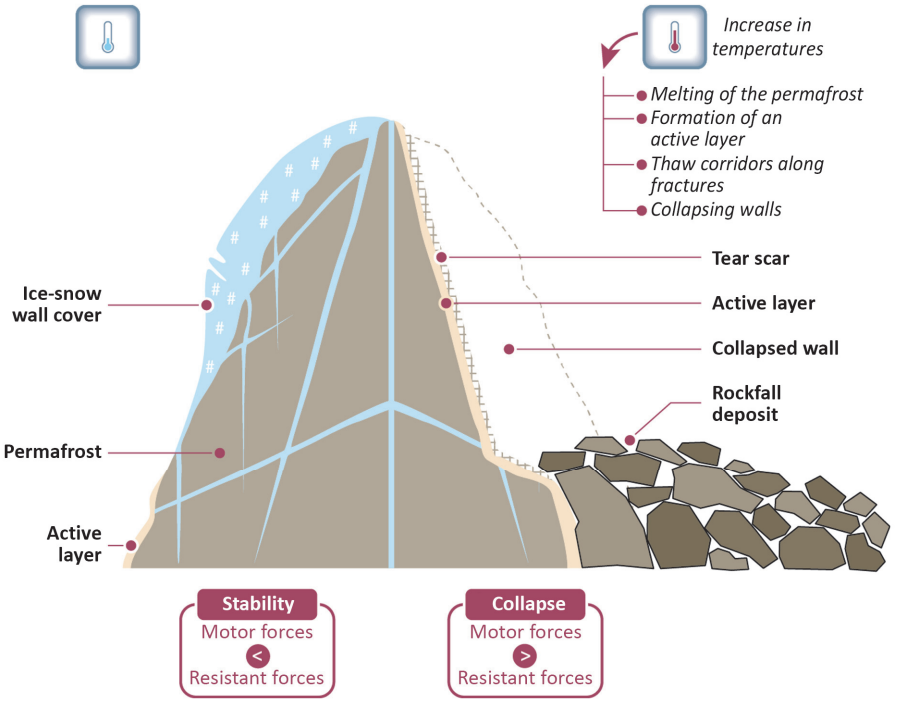

Figure 6.12. *Wall permafrost degradation causing gravity phenomena on high mountain slopes in the context of global warming (source: design D. Mercier, drawing F. Bonnaud, Sorbonne University; modified from Ravanel 2010)*

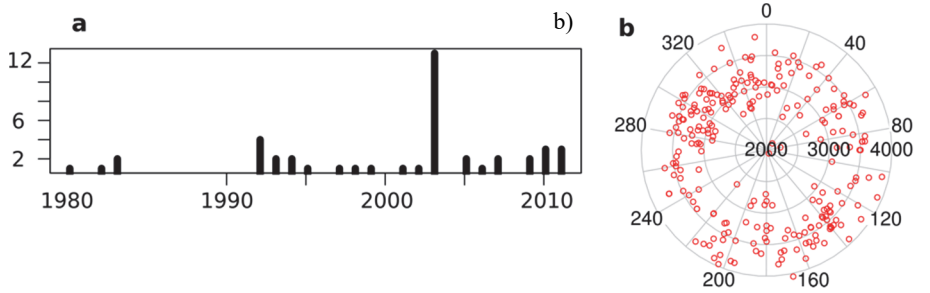

Figure 6.13. *(a) Annual number of collapses in the Aiguilles de Chamonix since 1980, established by photo comparison. (b) Altitude (in m) and orientation (in °) of all collapses recorded between 2007 and 2011 in the Mont Blanc massif (source: Ravanel and Deline 2015)*

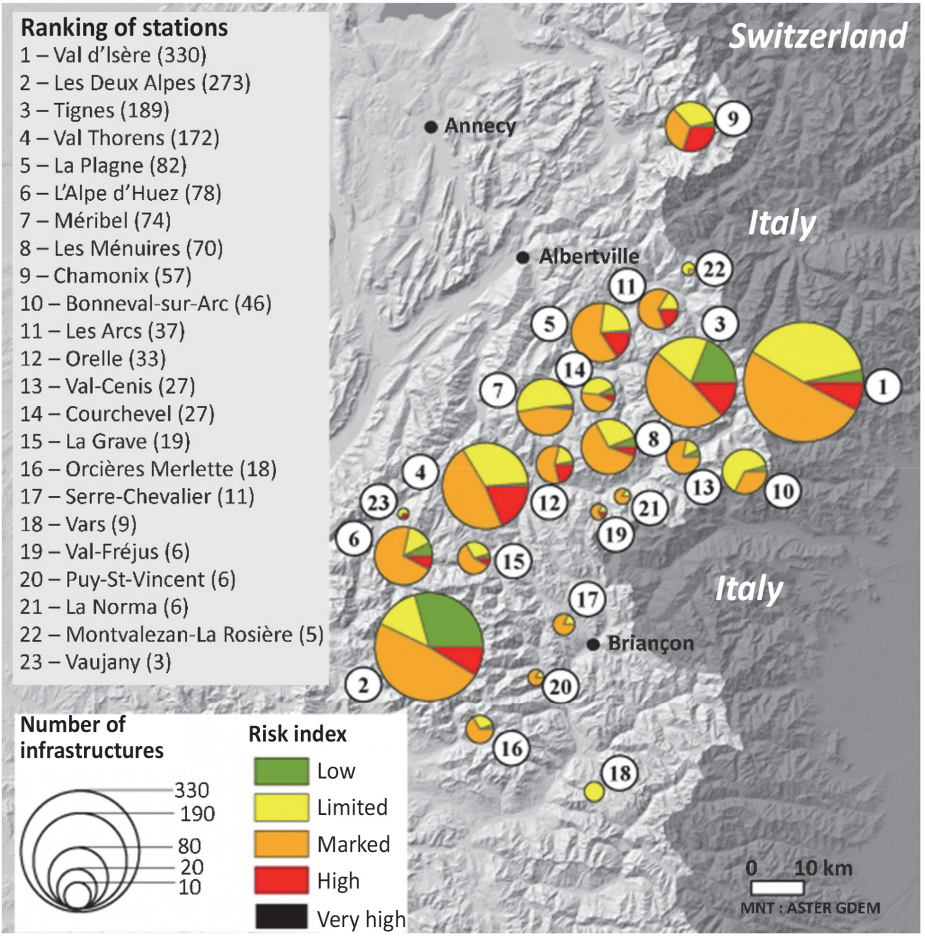

Figure 6.15. *Distribution of infrastructure at risk in stations of the French Alps (source: based on Duvillard* et al. *2015)*

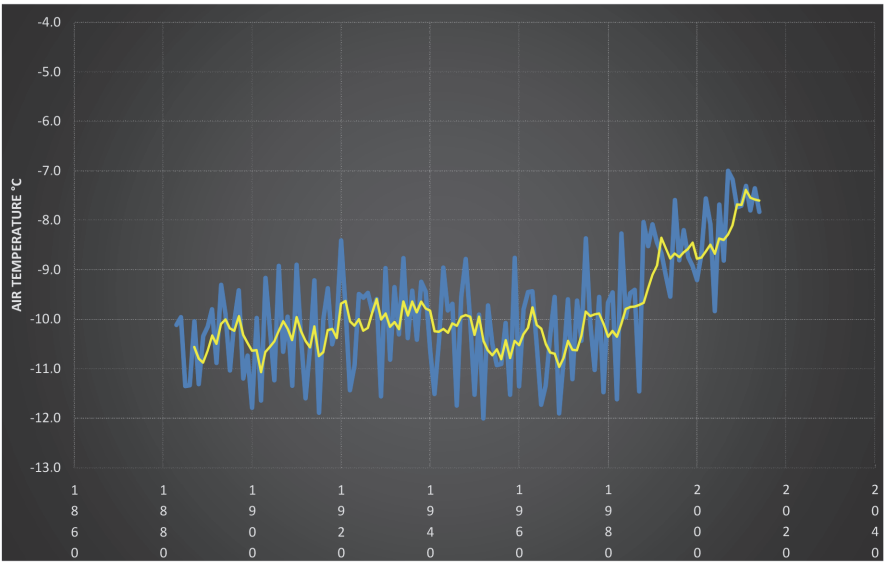

Figure 7.1. *Annual mean air temperatures at Yakutsk from 1880 to 2017 (Eastern Siberia, 62° 02′ N; 129° 42′ E, NOAA data). In blue: annual averages, in yellow: the five-year moving average*

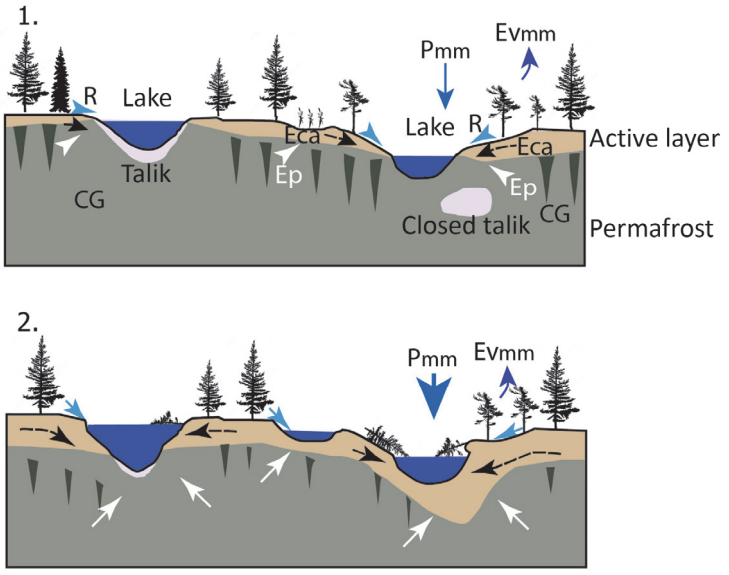

Figure 7.2. *Surface hydrologic functioning of permafrost zones: (a) undisturbed; (b) disturbed by climate change*

Figure 7.3. *Thermokarst depressions in Eastern Siberia (central from the main lake: 63° 51' 2.32" N – 123° 54' 54.47" E) (source: Google Earth)*

Figure 7.4. *Lake development related to the degradation of large permafrost ice wedges (Yakutia, north of Pokrovsk, May 2013). Polygonal soils bulge and depressions fill with water. As the wetland area expands, the spruce forest disappears. The level before collapse is shown by the arrow at the top right of the photograph (source: E. Gautier).*

Figure 7.5. *Baydjarakhs on the shore of a lake related to the degradation of large ice wedges in permafrost in Yakutia, Syrdak (source: photograph by F. Costard)*

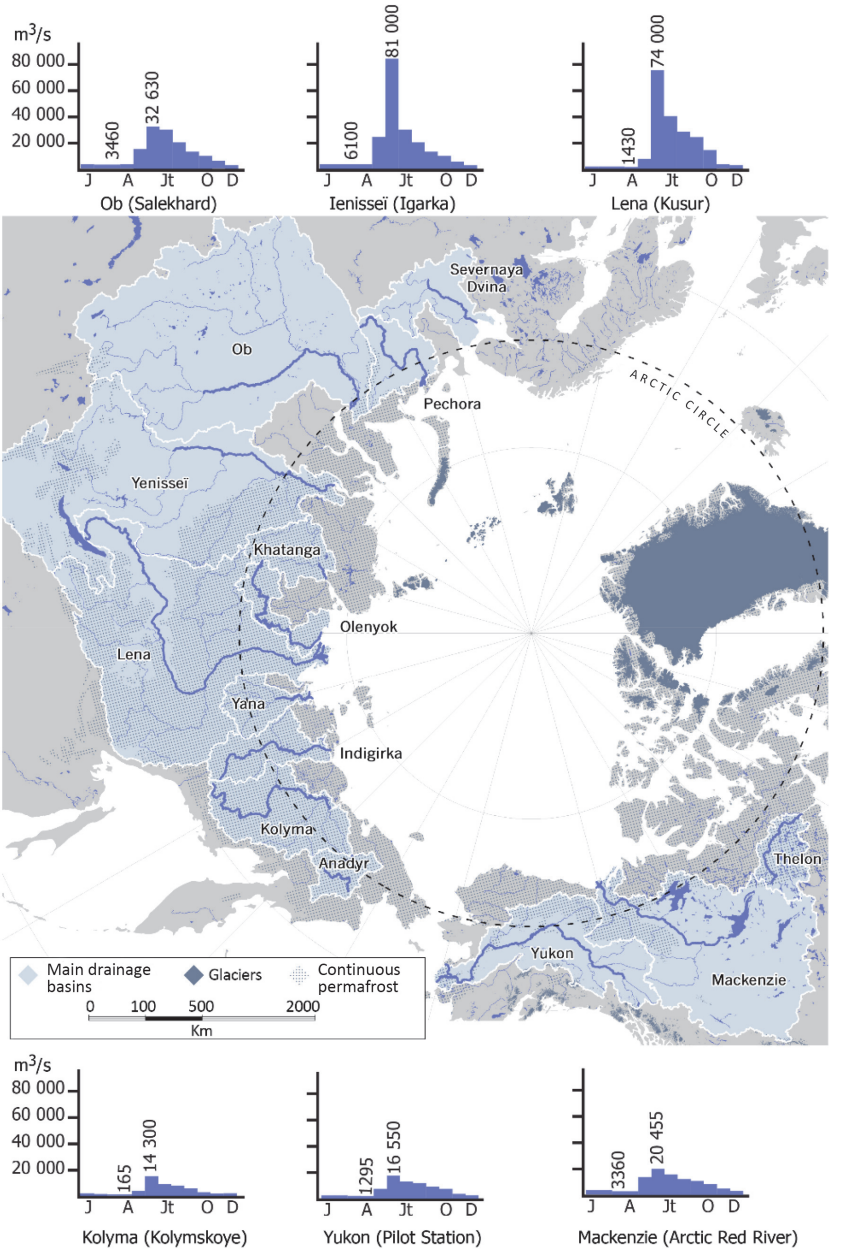

Figure 7.6. *Map of the main Arctic rivers with minimum and maximum monthly discharges (source: design E. Gautier; realization J. Cavero, 2019).*

Figure 7.7. *Lena in eastern Siberia in winter (source: photograph E. Gautier, April 2013)*

Figure 7.8. *Lena River in eastern Siberia – ice jam. The flood of May 2010 reached a historical level with more than 56,000 m^3 s^{-1} in Tabaga. The water level rose by more than 8 m in one night, the break-up was rapid and particularly damaging to the alluvial forest (source: photograph F. Costard, May 19, 2010).*

Figure 7.9. *Lena River in eastern Siberia – the consequences of the May 2010 ice breakup on alluvial vegetation. Note tree trunks broken cleanly by ice pans during breakup. In the background, willows, lying and partly buried under sandy deposits, are piled up and have made new stems (source: photograph E. Gautier, July 2010).*

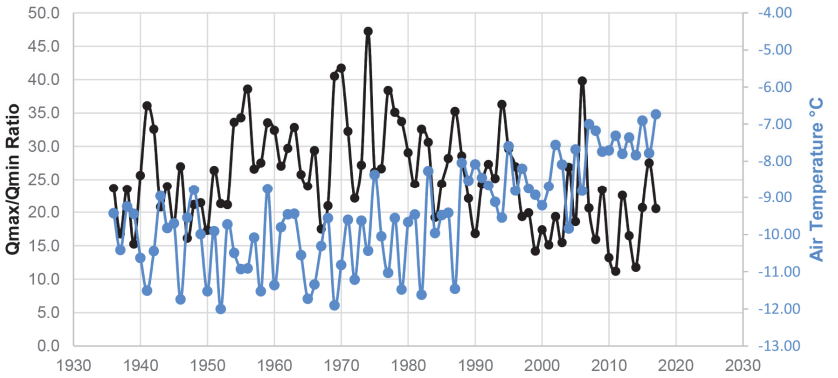

Figure 7.10. *The ratio between maximum and minimum water discharge rate (black curve) on the Lena River in eastern Siberia (Tabaga station, upstream of Yakutsk) and mean air temperatures at Yakutsk (blue curve) from 1936 to 2017 (source: adapted from Yang* et al. *2002; Ye et al. 2009; Gautier* et al. *2018)*

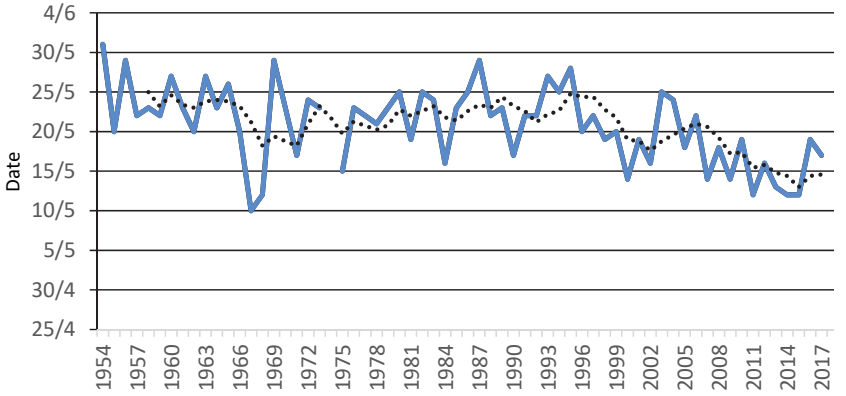

Figure 7.11. *Date of onset of breakup on the Lena at Tabaga in 1954 to 2017. In blue: date; dotted line: five-year moving average (source: adapted from Gautier* et al. *2018; Roshydromet data).*

Figure 7.12. *Flooding of the plain in May 2012 (Yakutia, upstream of Yakutsk) (source: photograph E. Gautier)*

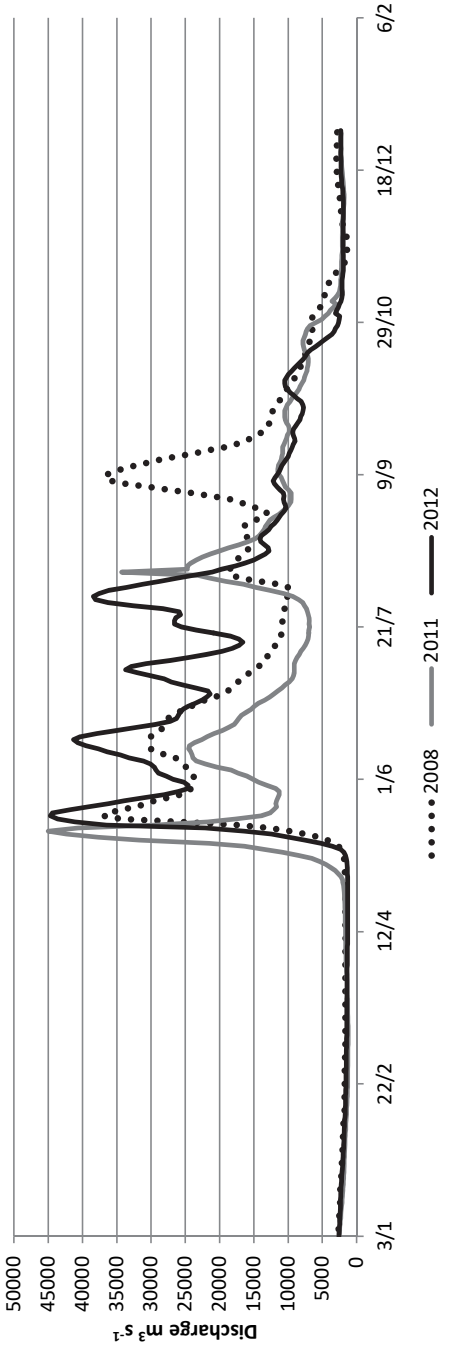

Figure 7.13. *Example of summer floods on the Lena at Tabaga (Roshydromet data)*

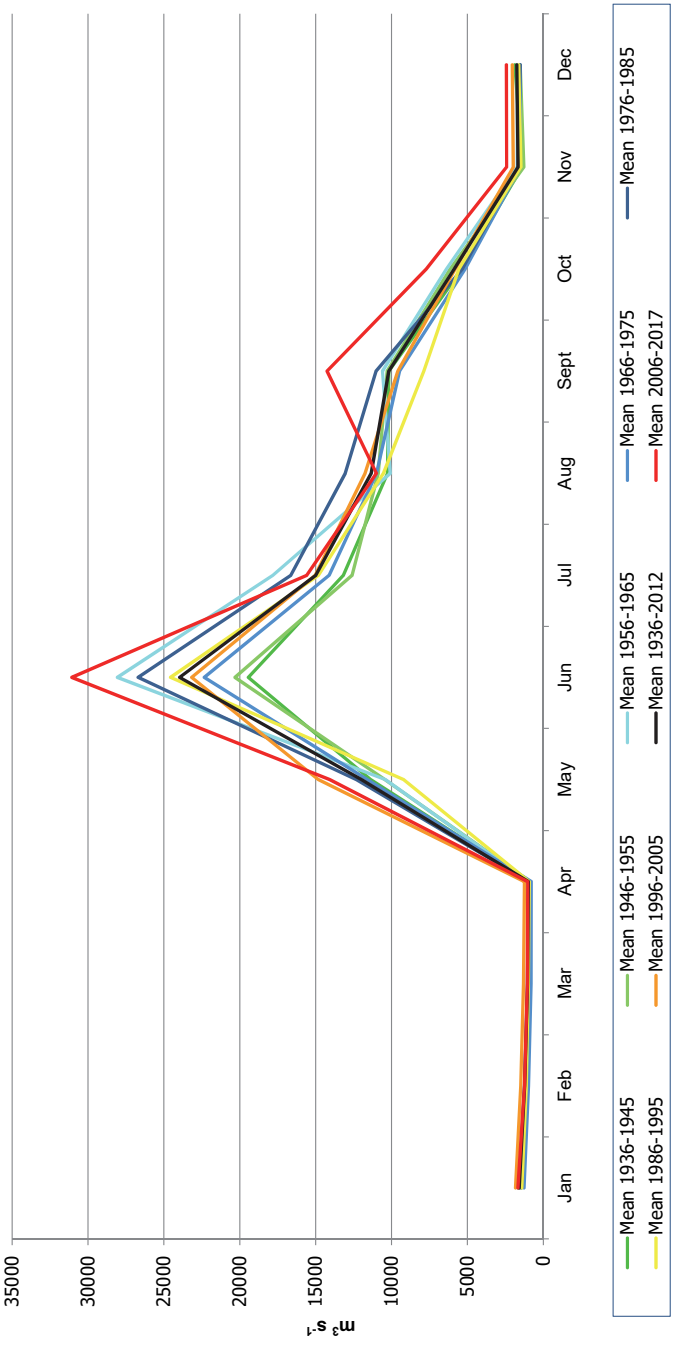

Figure 7.14. *Average monthly flows per decade from Lena to Tabaga station (1936–2017; Roshydromet data)*

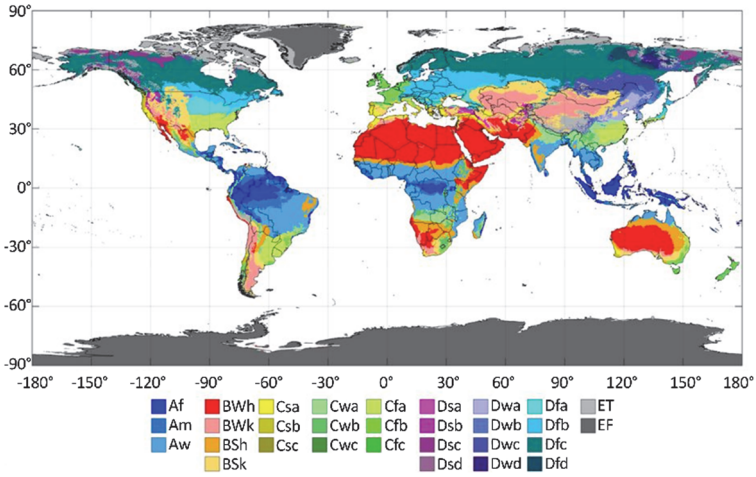

Figure 8.1. *The global climate mosaic according to the Köppen-Geiger classification. Map based on recorded climate data for the period 1980–2016 (source: Beck* et al. *2018)*

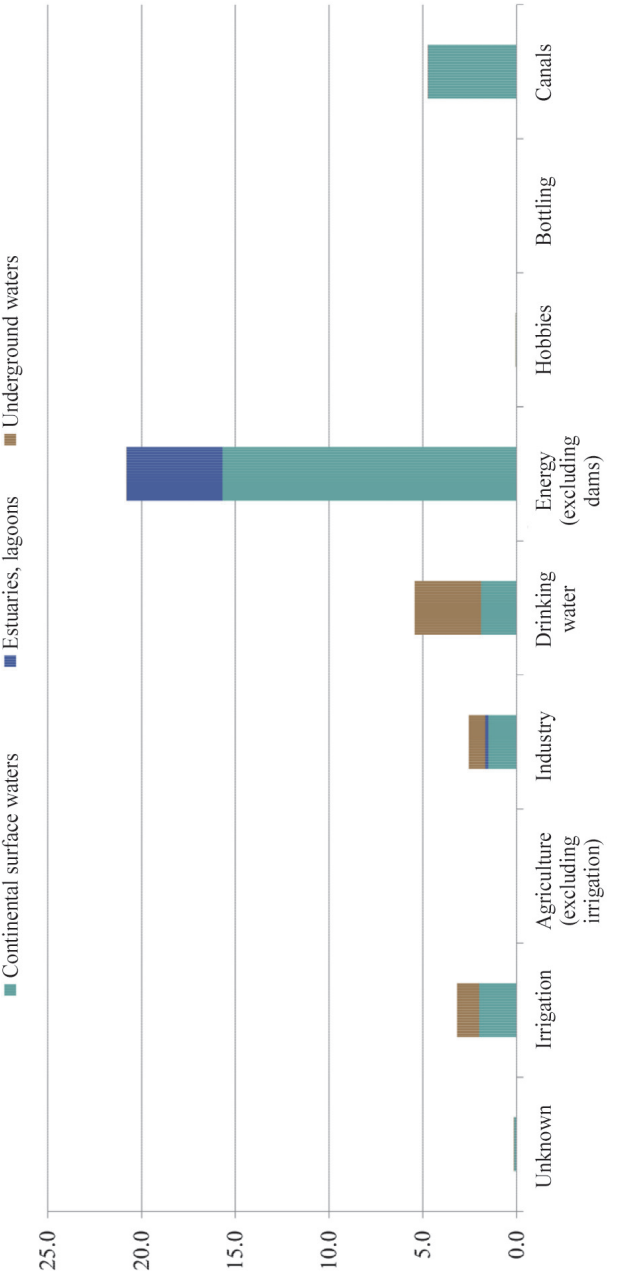

Figure 8.2. *Breakdown of the total volume of abstractions (in billions of m^3) according to the different uses declared and the type of water removed (mainland France and overseas territories). Data 2016 (source: Chataigner and Michon 2019)*

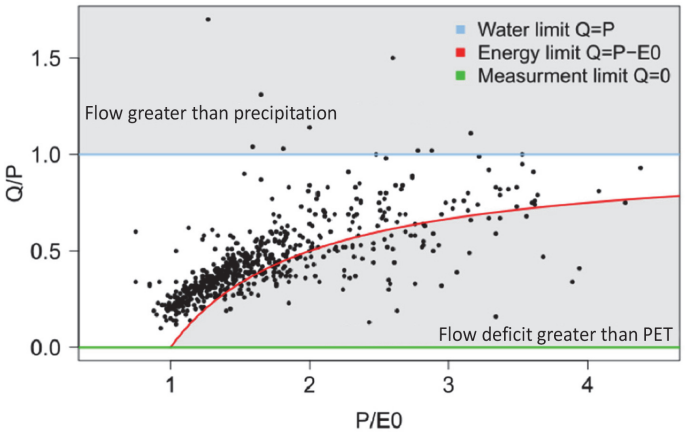

Figure 8.3. *Application of the dimensionless representation Q/P = f(P/PET) to a sample of 609 basins located in metropolitan France. On the graph: E0 = PET (source: Lebecherel 2015)*

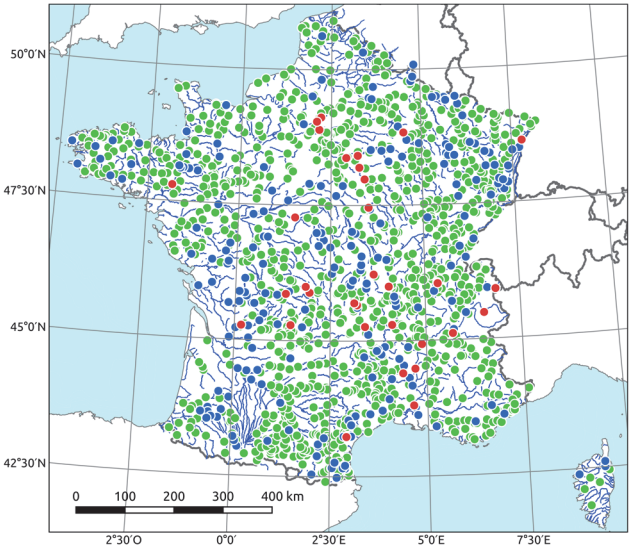

Figure 8.4. *Observation of daily flows*

Figure 8.5. *Flow observation station on the Moselle at Rupt-sur-Moselle (Vosges department, France); this station is part of the reference network for the climatic monitoring of low water levels (source: Vigicrues – DREAL GRAND EST)*

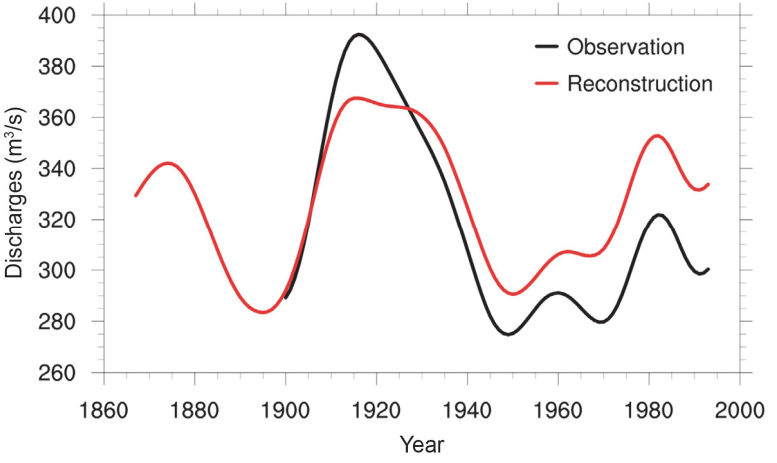

Figure 8.7. *Annual flows of the Seine in Paris (Austerlitz). In black the observations, in red a hydrometeorological reconstruction elaborated from different hypotheses. The curves are smoothed by a low-pass filter (source: Bonnet 2018)*

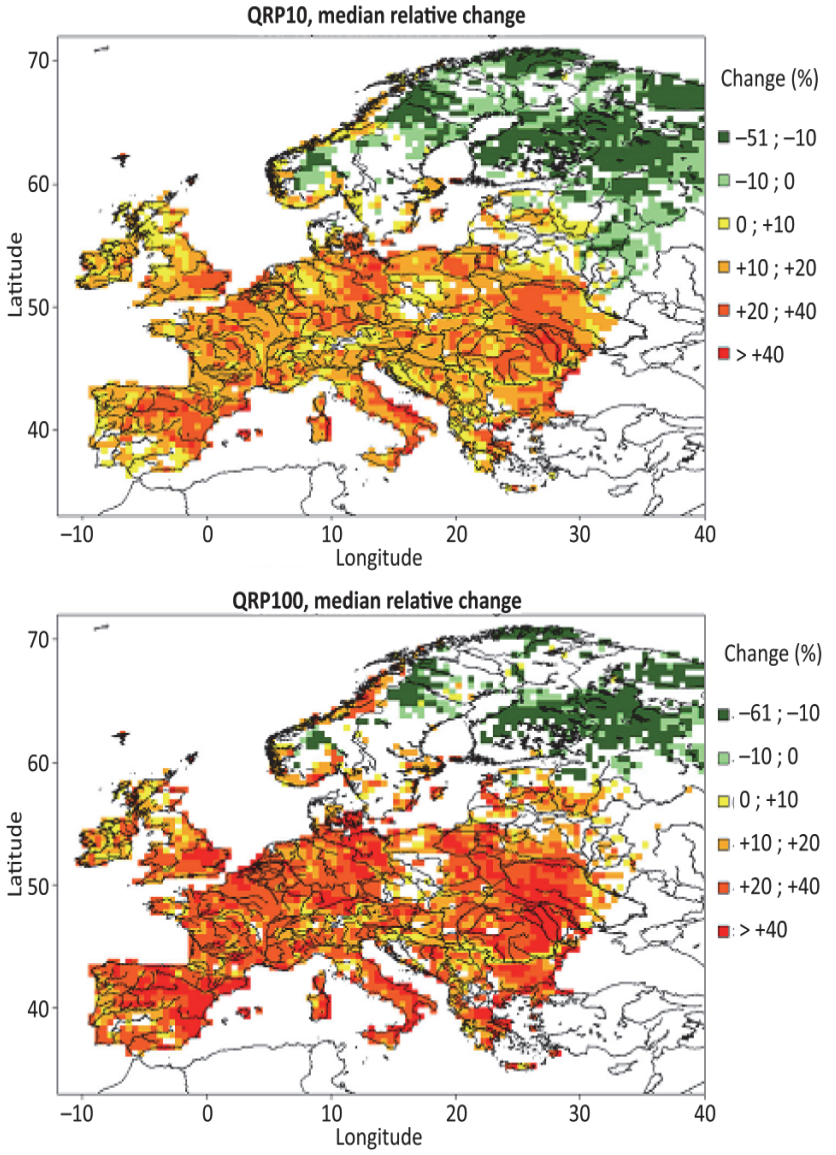

Figure 8.8. *Top: overall median (33 climate simulations) of the relative changes (%) in the annual maximum flood discharge that occurs on average once every 10 years. Bottom: overall median (11 climate simulations) of the relative change (%) in the annual maximum flood discharge that occurs on average once every 100 years. Only significant changes are shown in color (source: Roudier* et al. *2015).*

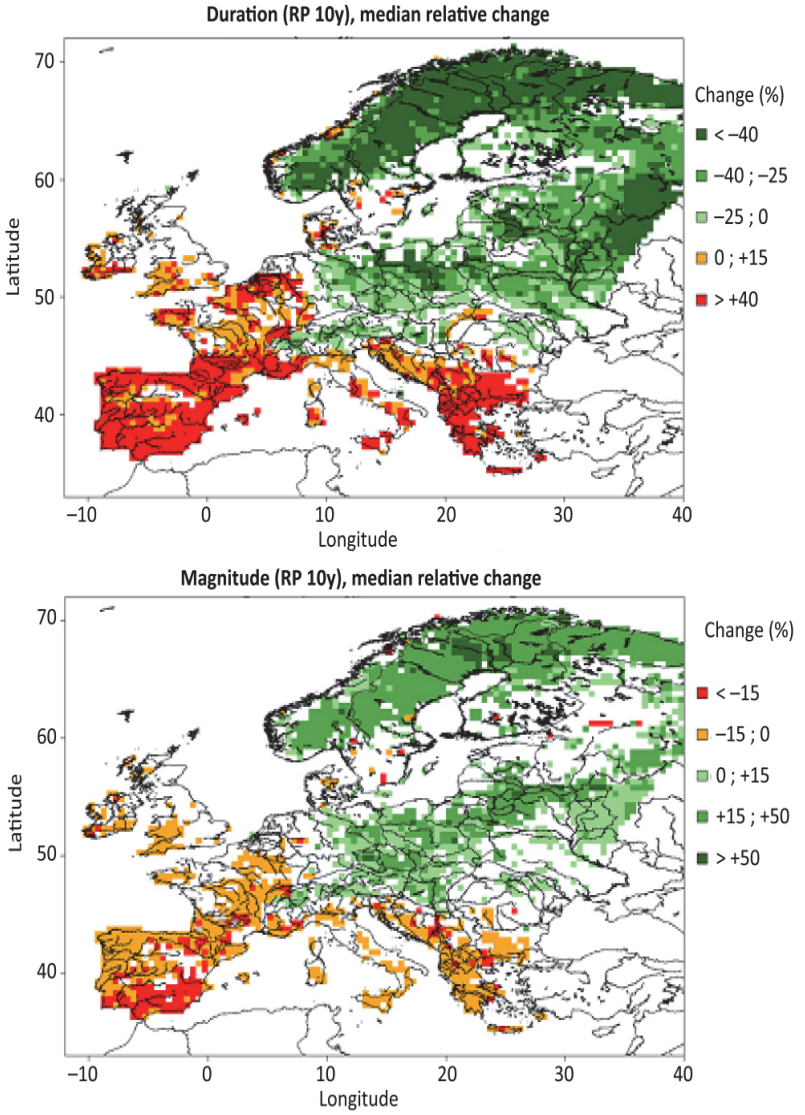

Figure 8.9. *Top: overall median (22 climate simulations) of the relative change (%) in the duration of low flow (here the 20th percentile of the classified flow curve) that occurs on average once every 10 years. Bottom: overall median (22 climate simulations) of the relative change (%) in the value of the low flow (20th percentile of the graded flow curve in this case) that occurs on average once every 10 years. Only significant changes are shown in color (source: Roudier* et al. *2015)*

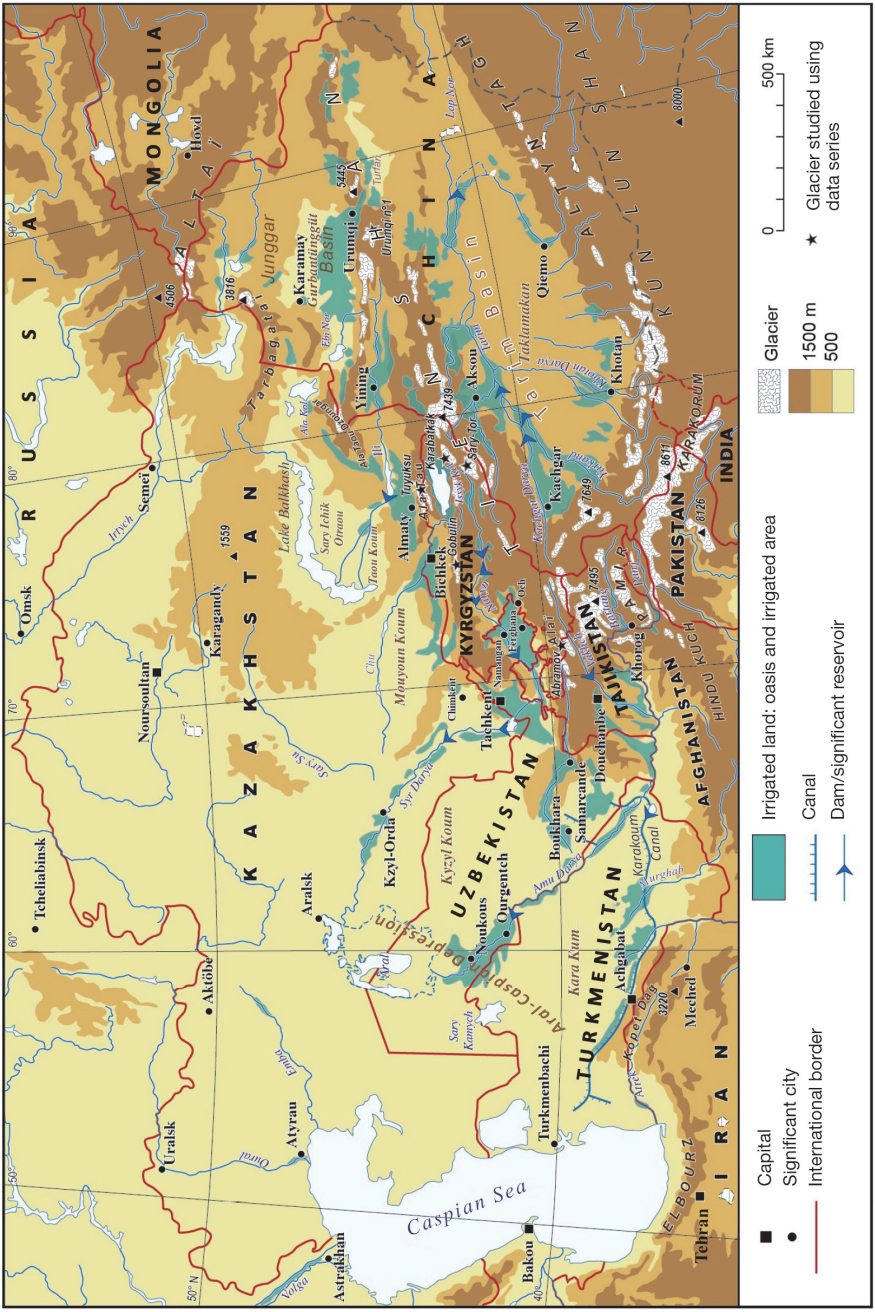

Figure 9.1. *Arid depressions fed by "water tower" mountains (source: Cariou 2019)*

Figure 9.2. *The Fedchenko glacier in the Pamir mountain range. Fed by multiple tributaries, the glacier covers an area of 579 km². Its altitude varies from 2,900 m at the terminal tongue to 6,300 m in the high basins dominated by Independence Peak (6,940 m). Its equilibrium line is located at an altitude of 4,700 m and the maximum thickness of the glacier reaches 1,000 m (source: photograph Knith 2011).*

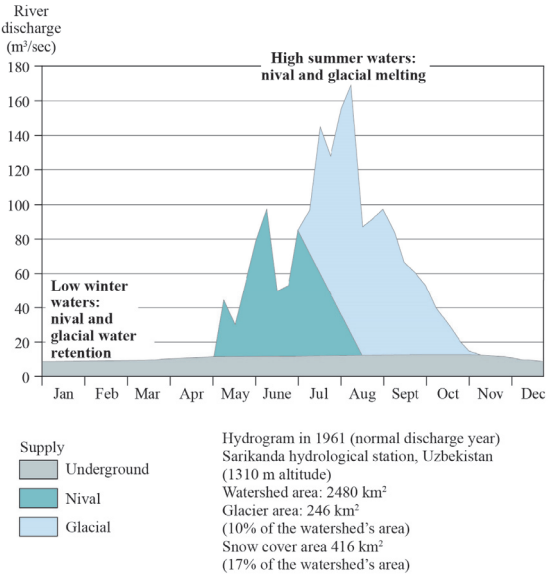

Figure 9.3. *Hydrological regime recharge patterns of the Sokh River (source: based on Kemmerikh 1972)*

A: Amu Darya regime and climatic regime in Kerki (station situated at the exit of the mountain, 180 m altitude and 1000 km from the mouth

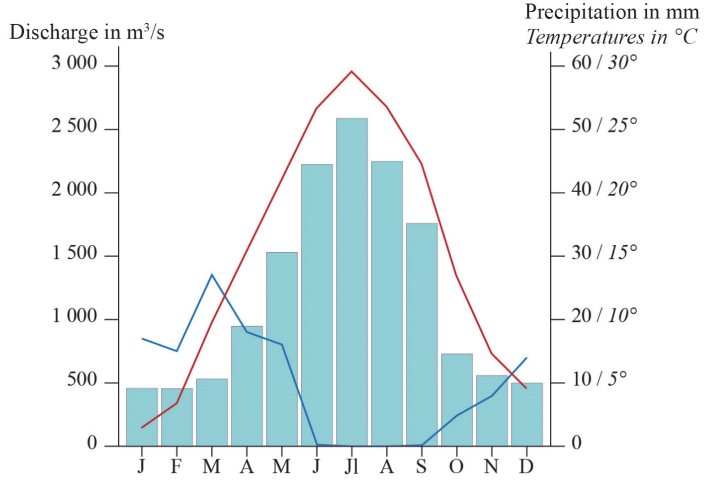

B: Tarim regime and climatic regime in Aller (station situated at the base of Tarim following the confluence of the rivers Asku, Yarkand and Khotan)

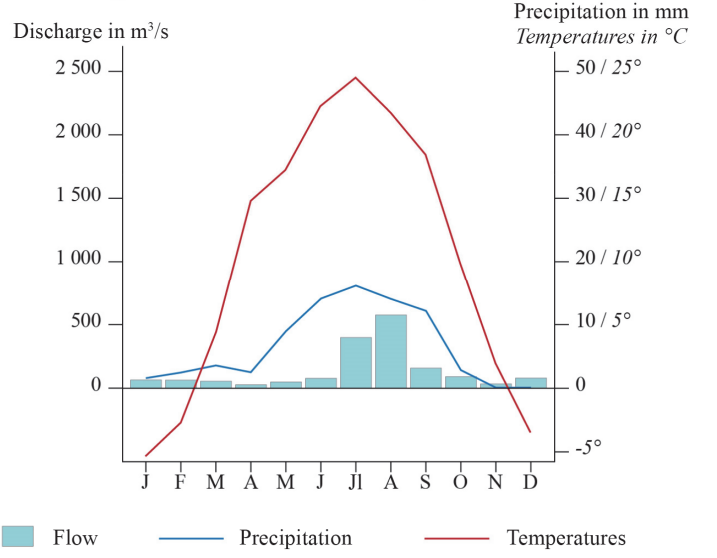

Figure 9.4. *Comparison of climatic and hydrological regimes in the Amu Darya and Tarim basin (source: Cariou 2019)*

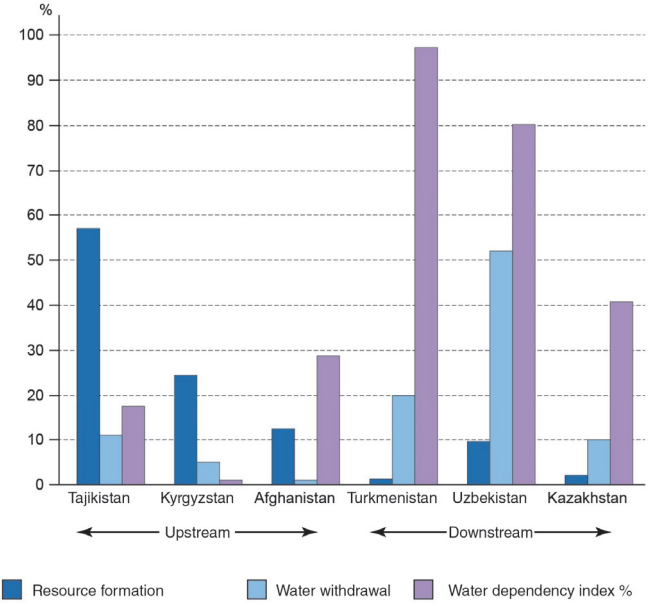

Figure 9.5. *Water resource formation and withdrawals in the Aral basin states (%) (source: based on data from Dukhovny and Sokolov 2003; Micklin 2002; Aquastat FAO 2015)*

Figure 9.6. *The Kirov Dam on the Talas River (Kyrgyzstan). Emblematic of the Soviet period, the dam was mainly built (1965–1975) to develop cotton cultivation. With a storage capacity of 0.55 km^3, it allows the irrigation of 220,000 hectares in Kyrgyzstan and 80,000 hectares in Kazakhstan (source: photograph by A. Cariou, 2014).*

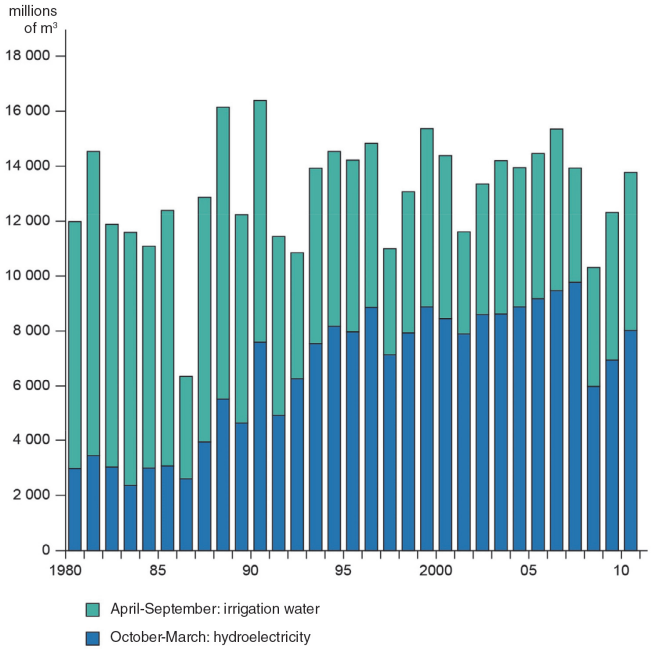

Figure 9.7. *Management of water releases from the Toktogul Dam in Kyrgyzstan (source: Global Water Partnership, 2014)*

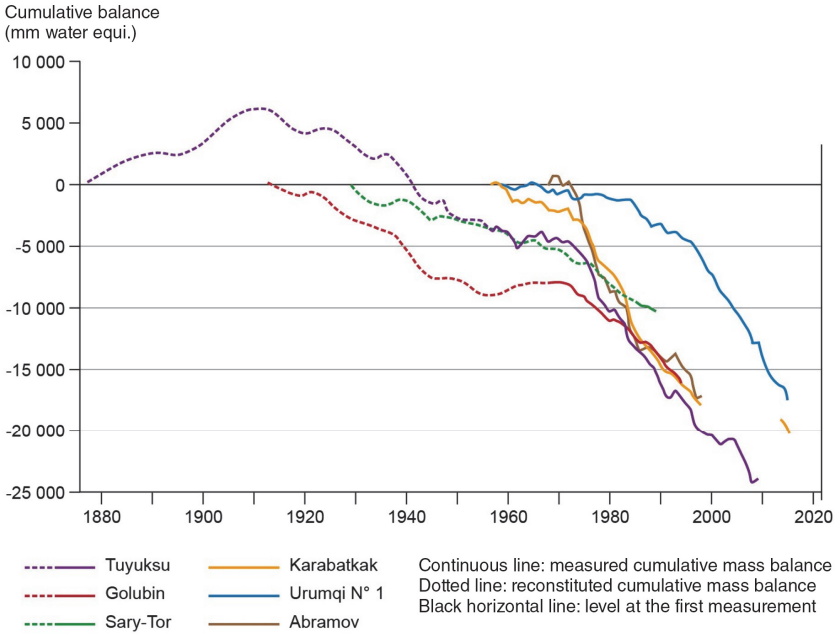

Figure 9.8. *Cumulative mean mass balances of six glaciers in the Tien Shan and Pamir mountain ranges (source: based on Sorg* et al. *2012; Hoelzle* et al. *2017)*

Figure 9.9. *The Tuyuksu glacier on the north slope of the Tien Shan (Zailiyskiy Alatau range). With a surface area of 5 km², the glacier is fed by a collector surrounded by peaks over 4,000 m high. Easily accessible, it has been the subject of regular observations since 1957. Since 1985, the glacier tongue has receded by more than 600 m (source: photograph by A. Cariou, 2017).*

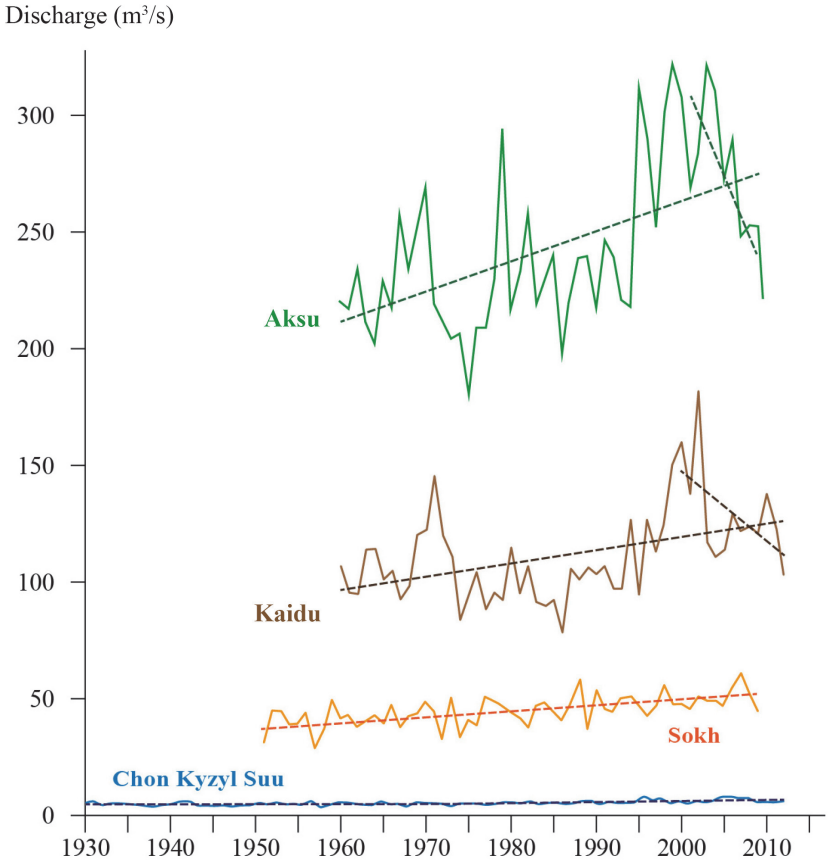

Figure 9.10. *Trends in mean annual flow of some Central Asian rivers (source: based on data from Bazanova and Ermenbaev 2015; Glazirin 2015; Deng 2019)*

Figure 9.11. *The Bartang River, a tributary of the upper Amu Darya River (Tajikistan). The incision of the rivers and the aridity of the Pamir valleys produce steep, bare slopes that are very sensitive to erosion and landslides at the slightest rainfall (source: photograph by A. Cariou, 2016)*

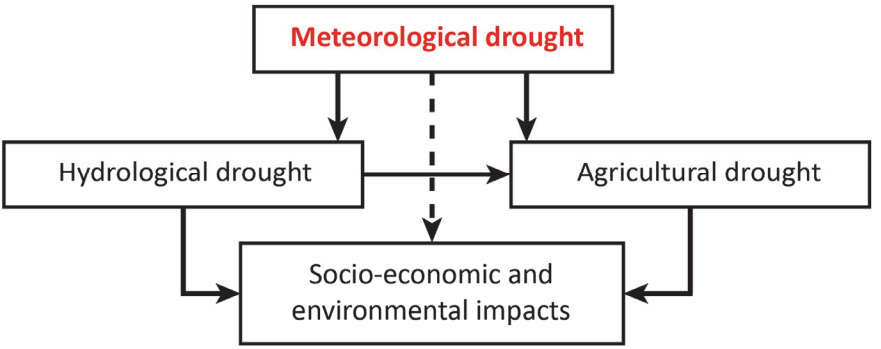

Figure 10.1. *Schematic representation of the different types of drought and their interactions, all of which result in socio-economic and environmental impacts (source: design and production F. Raymond).*

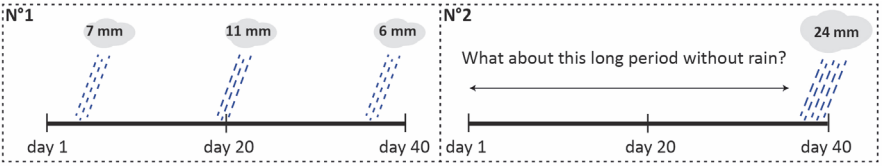

Figure 10.2. *Two so-called "dry" 40-day situations (N°1 and N°2), identical in terms of total rainfall received (24 mm) and number of dry days (37), but showing a significant difference in rainfall distribution (source: design and production F. Raymond)*

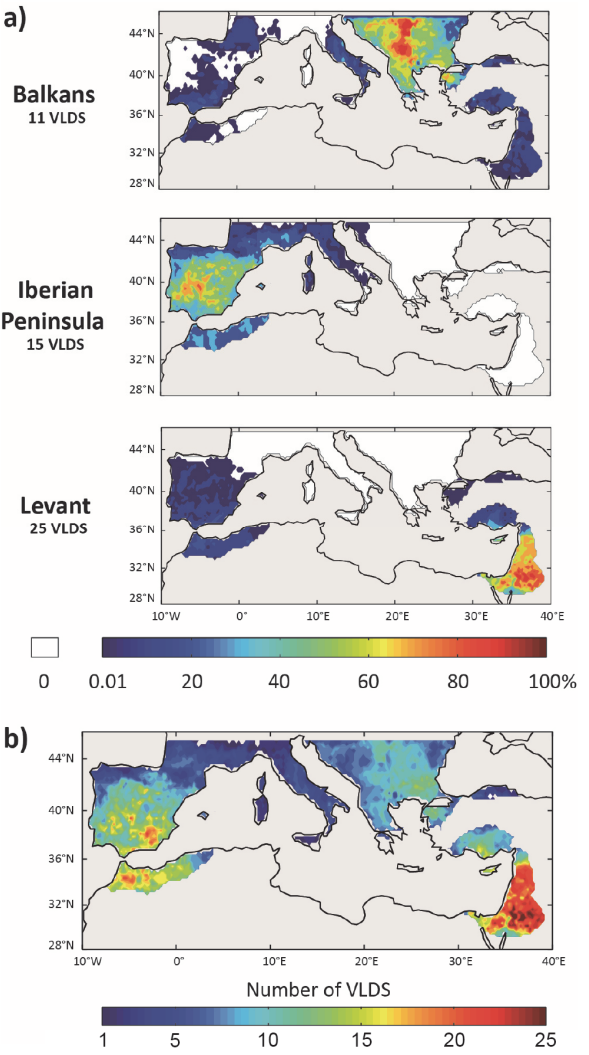

Figure 10.3. *(a) The three recurrent configurations of VLDS events observed in the Mediterranean basin since the 1950s: Balkans, Iberian Peninsula and the Levant. A percentage of 100% indicates that all the VLDS grouped in this configuration affect the sector in question. (b) Spatialization of the number of very long dry spell events observed over the whole of the Mediterranean territory studied since the 1950s (source: design and production F. Raymond)*

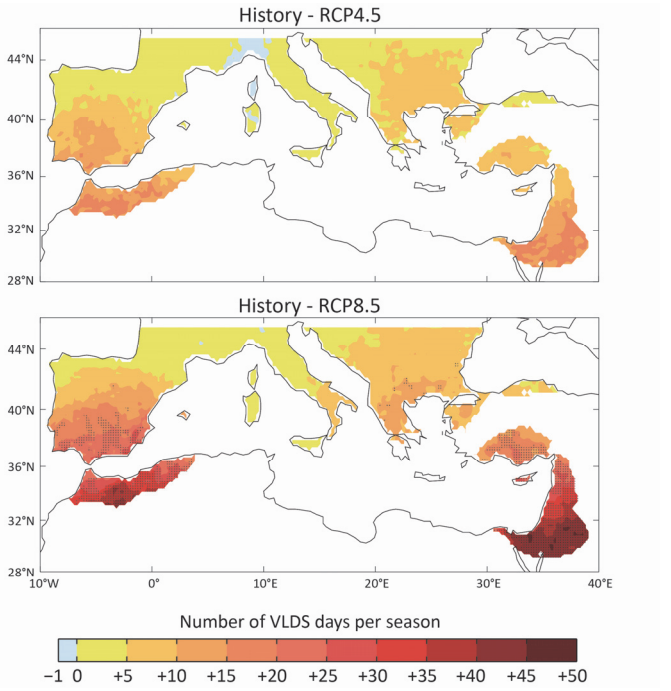

Figure 10.5. *Evolution of the average number of days of VLDS per rainy season for future trajectories (period 2066–2100) compared to the historical reference period (1971–2005)*

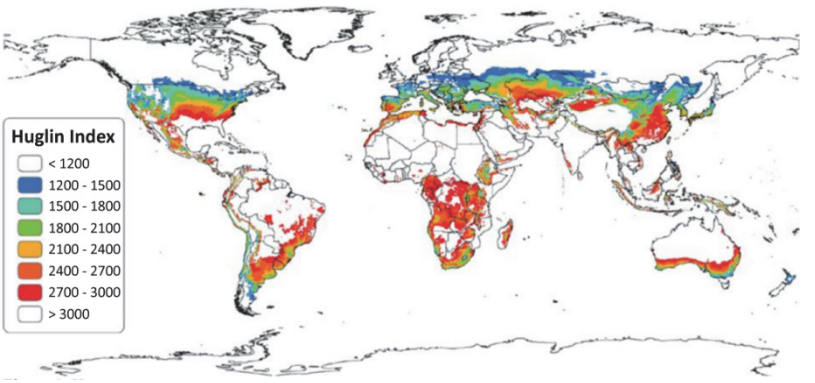

Figure 11.1. *Mapping of the average Huglin index for the world's wine-producing regions over the period 1950–2000 (Jones* et al. *2009) (source: Worldclim)*

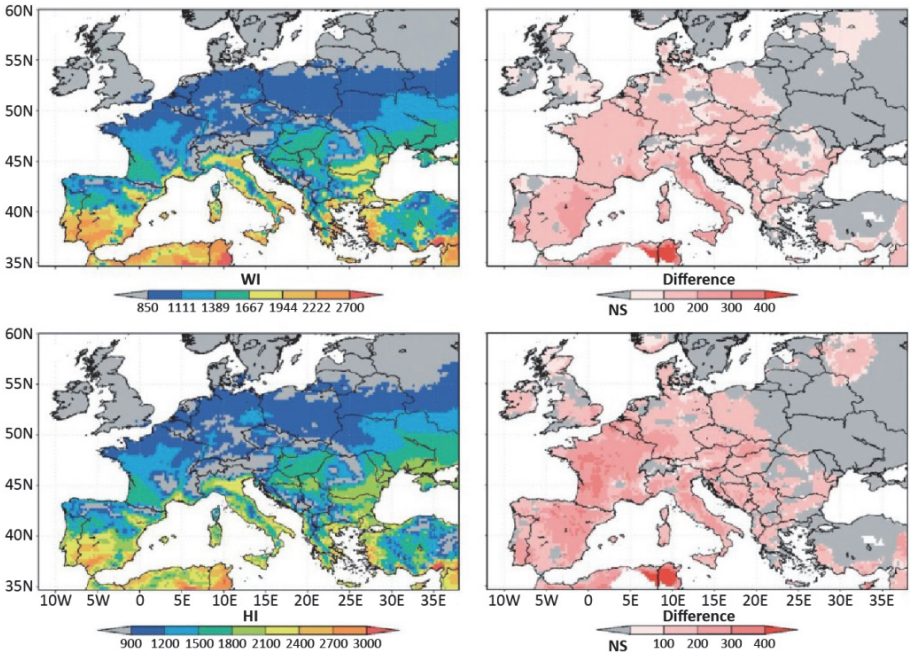

Figure 11.2. *(a) and (c) show the Winkler and Huglin indices in Europe over the period 1950–2009. (b) and (d) show the difference, for each index, between 1950–1979 and 1980–2009 (source: Santos* et al. *2012).*

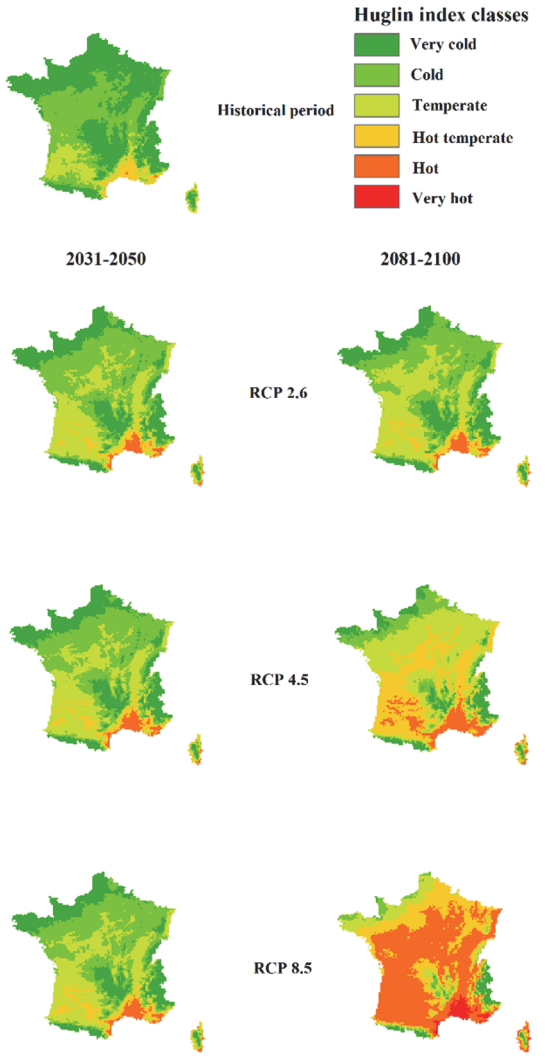

Figure 11.3. *Huglin index modeled on France over the periods 1986–2005, 2031–2050 and 2081–2100 under RCP scenarios 2.6, 4.5 and 8.5 with a spatial resolution of 8 km (sources: DRIAS).*

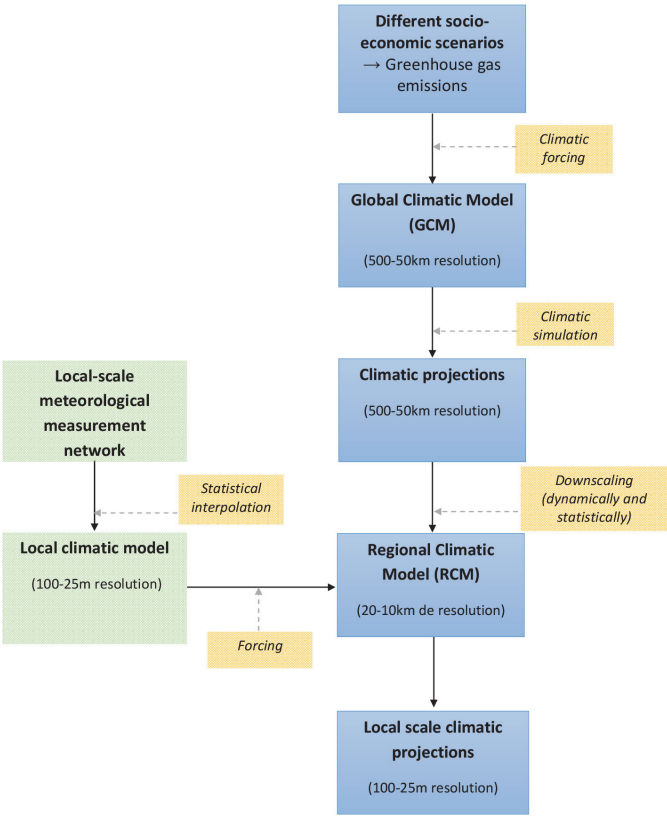

Figure 11.4. *Different stages of downscaling (from global to local) climate change projections (source: adapted from Daniels* et al. *2012)*

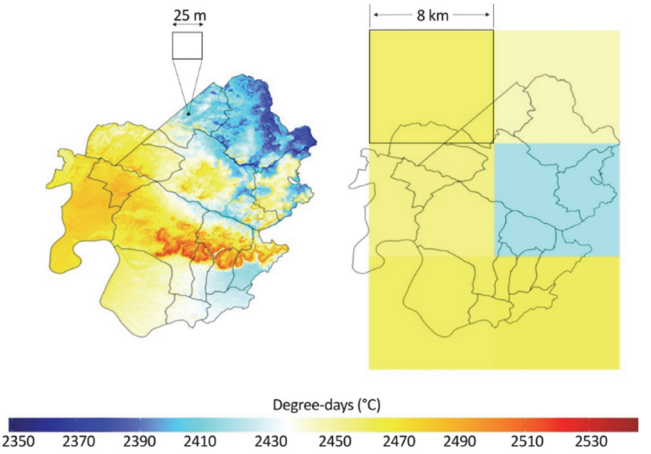

Figure 11.5. *Spatialization of the Winkler index in the Pomerol/Saint-Émilion region with a resolution of 8 km (rudder mesh, right) and at a resolution of 25 m (left) according to the RCP 8.5 scenario for the period 2081–2100 (source: adapted from Le Roux* et al. *2017)*

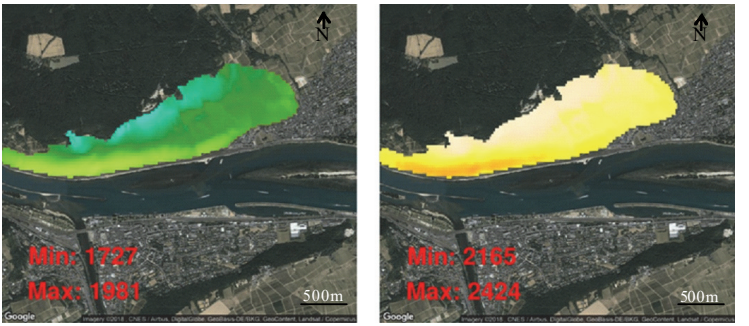

(2031-2050) (2081-2100)

Figure 11.6. *Modeling of the spatial variability of the Huglin index at the local scale in Rheingau vineyards (Germany) according to the RCP 8.5 scenario*

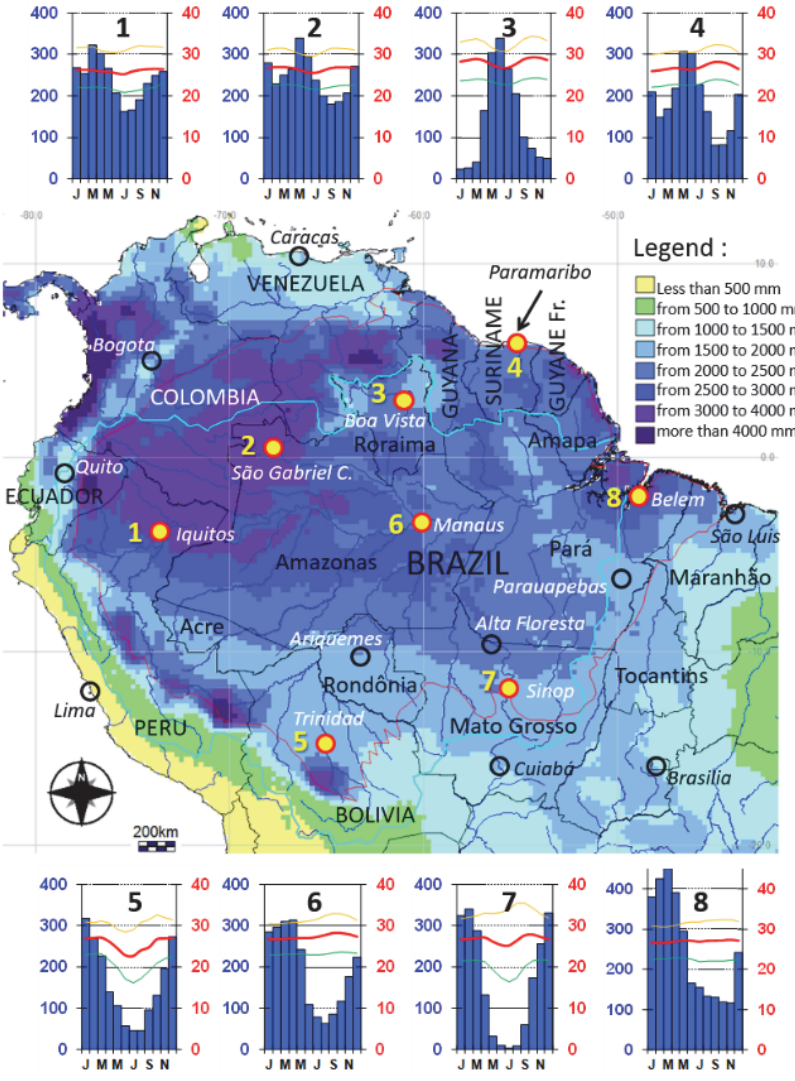

Figure 12.1. *Location and synthesis map of the Amazonian climate*

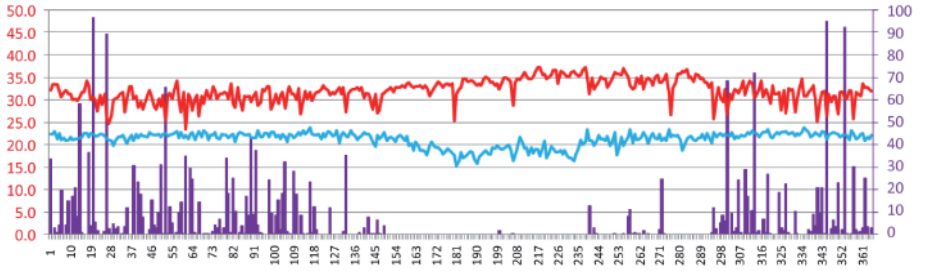

Figure 12.2. *Daily temperature and precipitation in Alta Floresta (Mato Grosso) in 2014: minimum temperature (in degrees) in blue, maximum in red and precipitation (in millimeters) in violet (source: designed and created by the authors)*

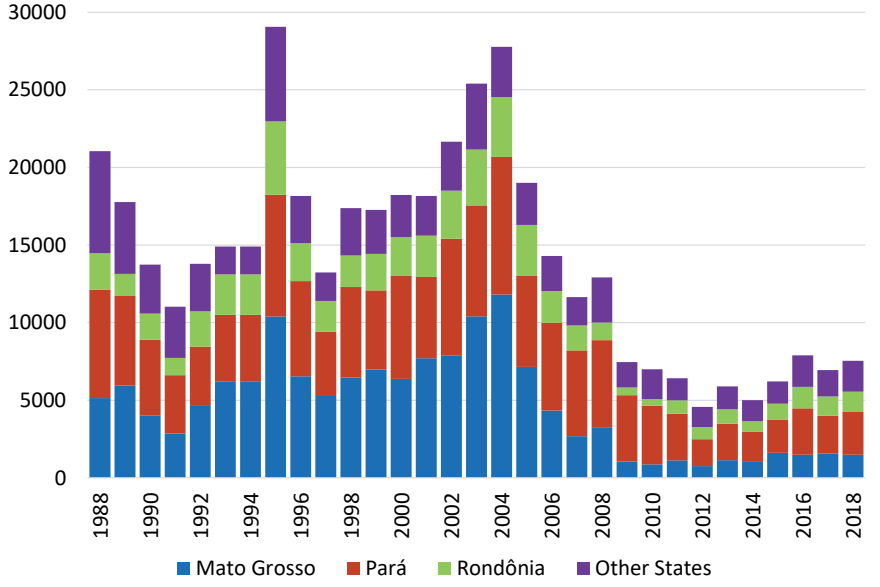

Figure 12.3. *Annual deforestation in the Brazilian Amazon in km^2 (source: INPE 2019)*

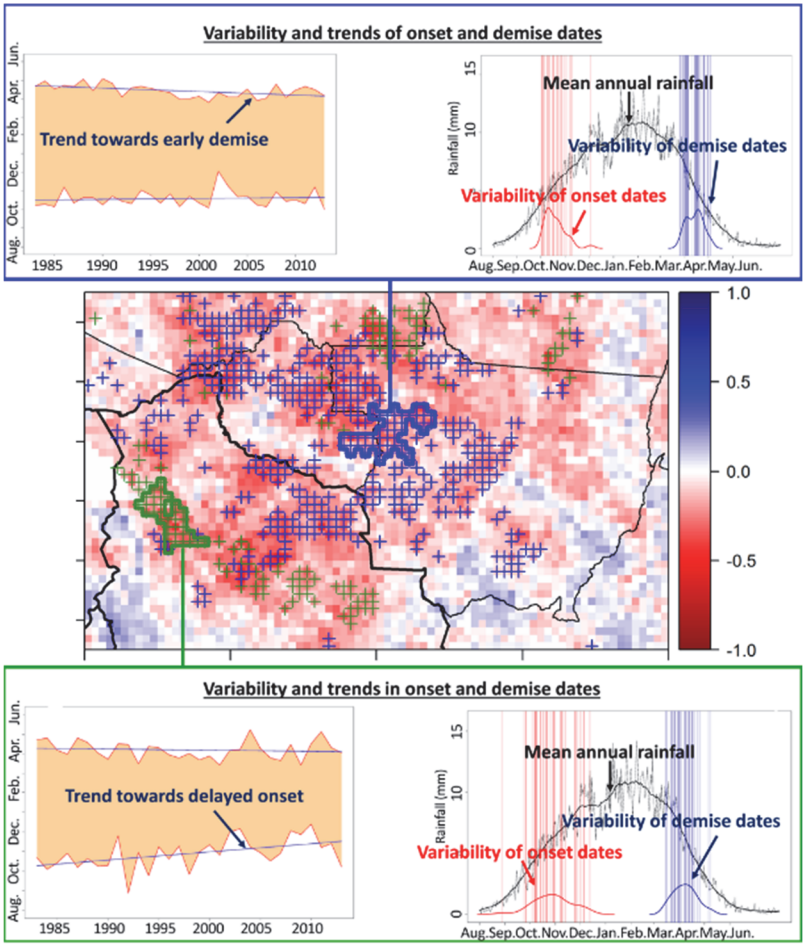

Figure 12.4. *Evolution of rainy season onset and demise dates in the southern Amazon from 1983 to 2014*

Figure 12.5. *Temperatures (left, in°C) and relative humidity (right, in %) from June 2013 to May 2014 in Alta Floresta (Mato Grosso) for different land use types (source: based on Dubreuil* et al. *2015).*

Time	J	F	M	A	M	J	J	A	S	O	N	D	AN
00:00	1.1	0.5	1.1	1.4	2.8	2.3	1.9	3.2	2.0	1.7	0.7	0.9	**1.6**
01:00	1.0	0.5	1.1	1.2	2.7	2.3	2.2	3.2	2.0	1.7	0.6	0.9	**1.6**
02:00	0.9	0.4	0.9	1.2	2.5	2.2	2.6	3.2	2.0	1.6	0.6	0.8	**1.6**
03:00	0.8	0.4	0.9	1.1	2.4	2.2	2.8	3.3	2.1	1.6	0.5	0.9	**1.6**
04:00	0.8	0.4	0.8	1.0	2.2	2.1	2.8	3.4	2.2	1.5	0.4	0.8	**1.5**
05:00	0.8	0.4	0.8	1.0	2.1	2.1	2.8	3.4	2.2	1.4	0.4	0.8	**1.5**
06:00	0.8	0.4	0.7	0.9	2.0	1.9	2.7	3.4	2.1	1.2	0.3	0.6	**1.4**
07:00	1.1	0.5	1.0	1.2	2.6	2.1	2.6	2.8	1.7	0.7	0.4	0.8	**1.5**
08:00	1.1	0.4	1.3	1.0	2.0	3.0	2.4	0.8	0.0	0.1	0.0	0.1	**1.0**
09:00	0.3	-0.3	0.6	0.5	0.9	1.8	1.1	-0.2	-0.7	-0.3	-0.4	-0.4	**0.2**
10:00	-0.4	-0.6	0.2	0.2	0.4	0.6	0.2	-0.7	-1.3	-0.6	-0.5	-0.6	**-0.3**
11:00	-0.4	-0.7	0.1	0.2	0.0	-0.1	-0.3	-0.7	-1.1	-0.6	-0.4	-0.6	**-0.4**
12:00	-0.7	-1.1	-0.1	0.4	0.5	-0.1	-0.3	-0.7	-1.1	-0.3	-0.9	-0.4	**-0.4**
13:00	-0.3	-0.8	0.0	0.1	0.3	-0.1	-0.5	-0.5	-1.1	0.0	-0.8	-0.6	**-0.4**
14:00	-0.8	-1.0	-0.6	0.2	0.5	0.0	-0.2	-0.3	-0.8	0.9	-0.7	-0.4	**-0.3**
15:00	-0.6	-0.6	0.0	0.5	1.0	0.0	0.0	0.7	-0.5	1.5	0.1	-0.1	**0.2**
16:00	-0.3	-0.1	0.8	0.6	1.2	0.5	0.6	1.2	0.5	2.1	0.4	0.4	**0.7**
17:00	0.0	0.1	1.3	1.0	1.4	1.2	1.4	2.9	1.1	2.2	0.9	0.7	**1.2**
18:00	0.6	0.2	1.3	1.5	2.5	2.1	2.6	4.7	1.9	2.4	1.1	1.0	**1.8**
19:00	1.3	0.7	1.8	2.2	3.5	3.2	3.5	4.9	2.2	2.3	1.4	1.4	**2.3**
20:00	1.7	0.6	2.0	2.3	3.6	3.2	3.1	4.2	2.1	2.2	1.4	1.5	**2.3**
21:00	1.7	0.6	1.8	2.1	3.3	2.9	2.3	3.6	2.1	2.3	1.2	1.3	**2.1**
22:00	1.7	0.6	1.6	1.9	3.0	2.7	1.9	3.2	1.9	2.1	1.0	1.2	**1.9**
23:00	1.3	0.4	1.3	1.6	2.7	2.4	1.8	3.0	2.0	2.0	0.8	1.1	**1.7**
00:00	1.1	0.4	1.1	1.4	2.7	2.4	1.9	3.1	1.9	1.7	0.7	1.0	**1.6**
	0.6	**0.1**	**0.9**	**1.1**	**1.9**	**1.7**	**1.7**	**2.2**	**1.0**	**1.3**	**0.4**	**0.5**	**1.1**

Figure 12.6. *Urban heat island intensity in Sinop in 2018: average temperature difference (in degrees) per hour (row) and per month (column) between the center and the periphery (source: designed and created by the authors)*

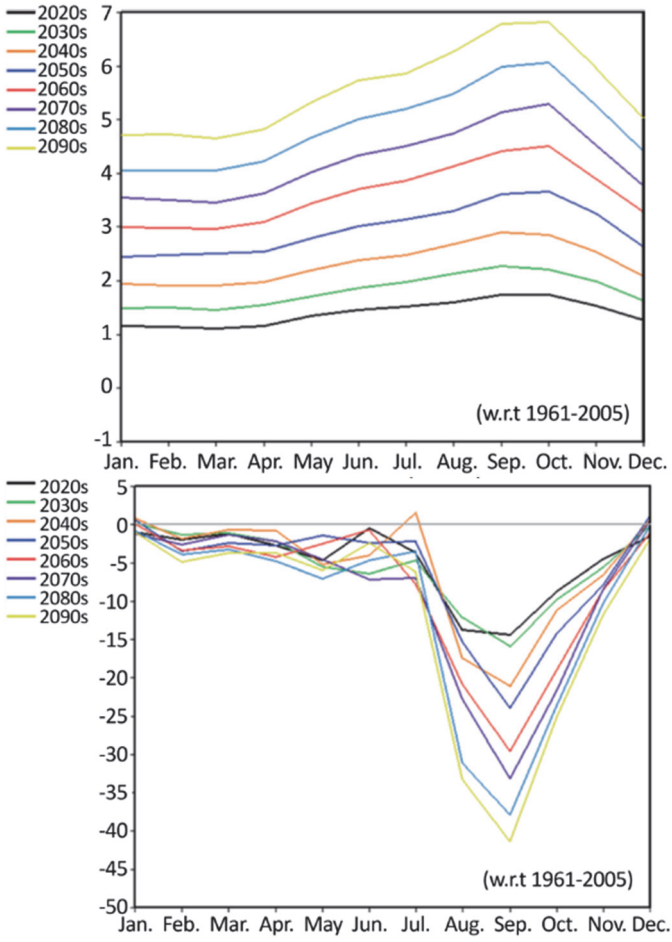

Figure 12.7. *Multi-model averages of the projected change in air temperature (top,°C) and precipitation (bottom, %) in the southern Amazon for the RCP8.5 scenario per decade over the period 2020–2100 relative to the baseline period 1961–2005 (source: Sampaio* et al. *2018)*

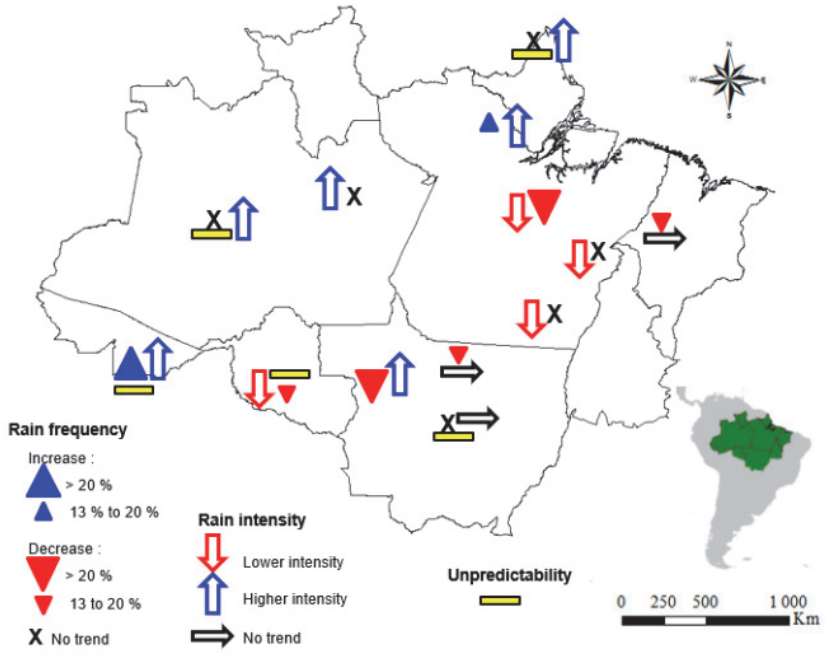

Figure 12.8. *Synthesis of perceptions of climate change in 13 Amazonian communities (source: based on Funatsu* et al. *2019)*

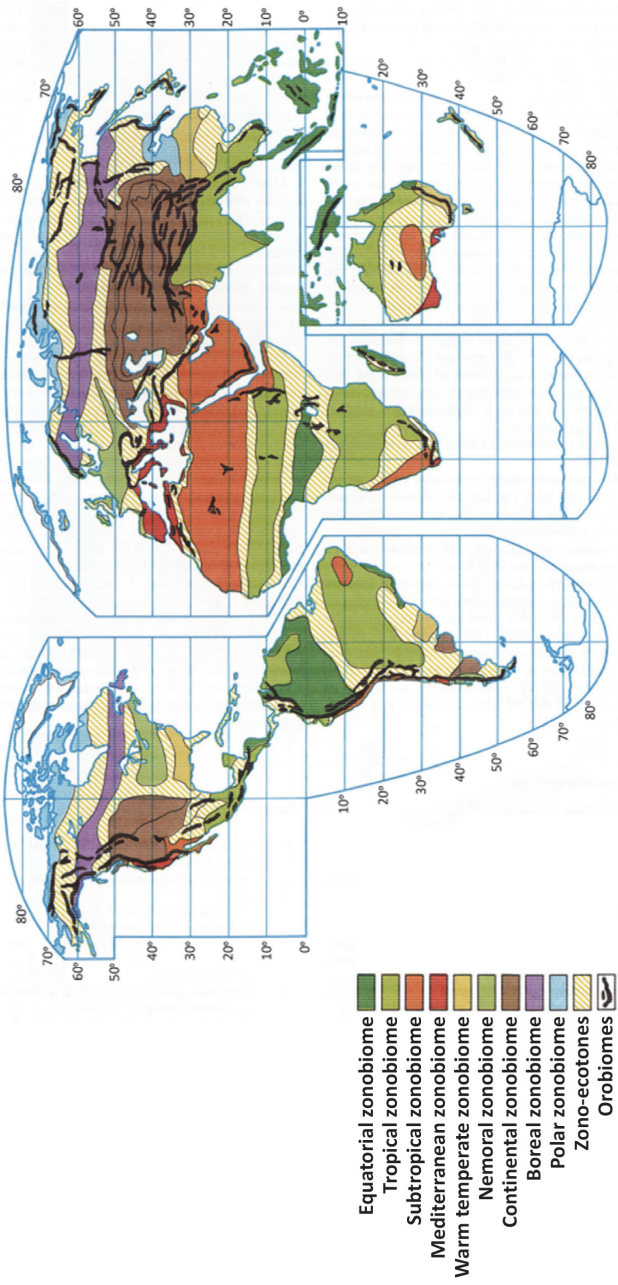

Figure 13.1. *Global map of terrestrial zonobiomes according to Walter (1976) classification (source: Heinrich and Hergt 1993)*

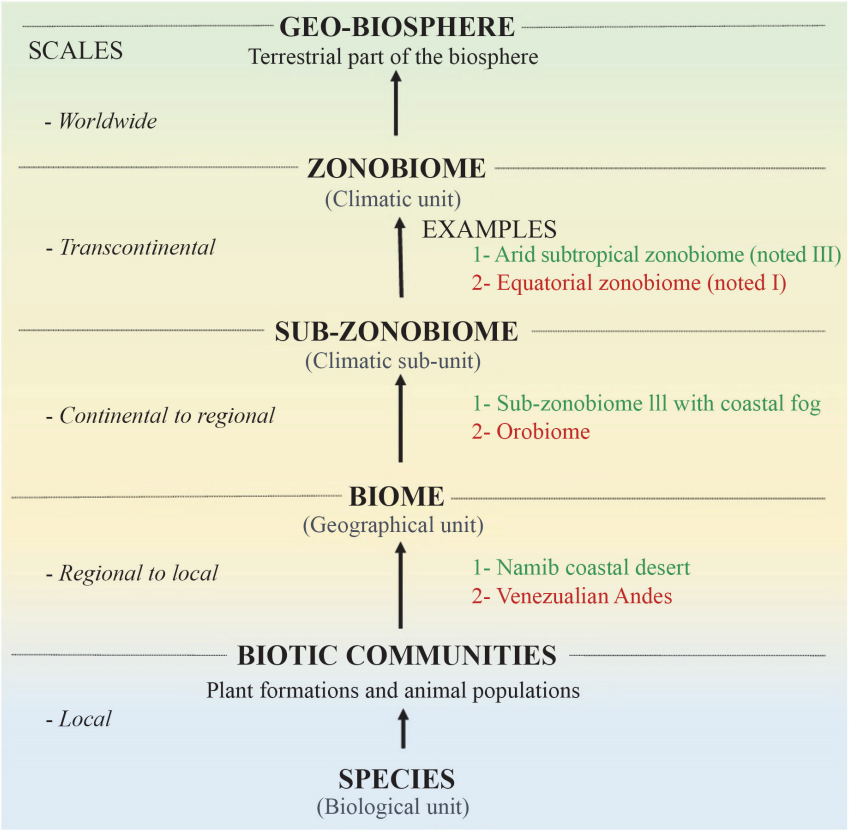

Figure 13.2. *From zonobiomes to biomes: a hierarchy of concepts (source: Mucina 2019, modified from Walter and Box 1976)*

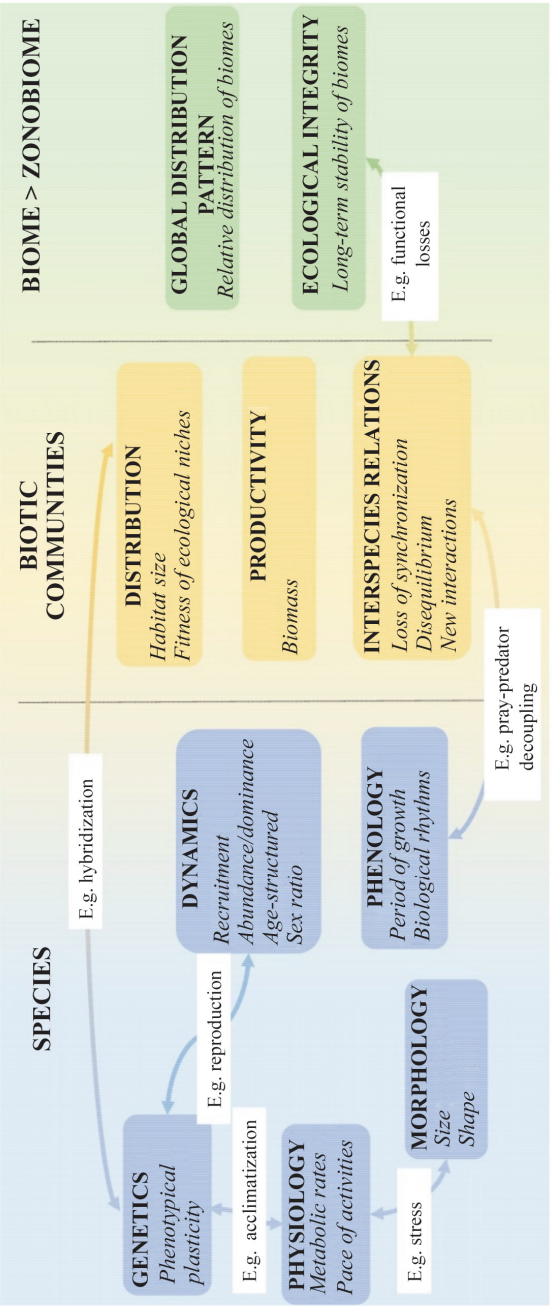

Figure 13.3. *Types of major impacts identified on terrestrial biomes and hierarchical scale involved (source: design and production D. Gramond)*

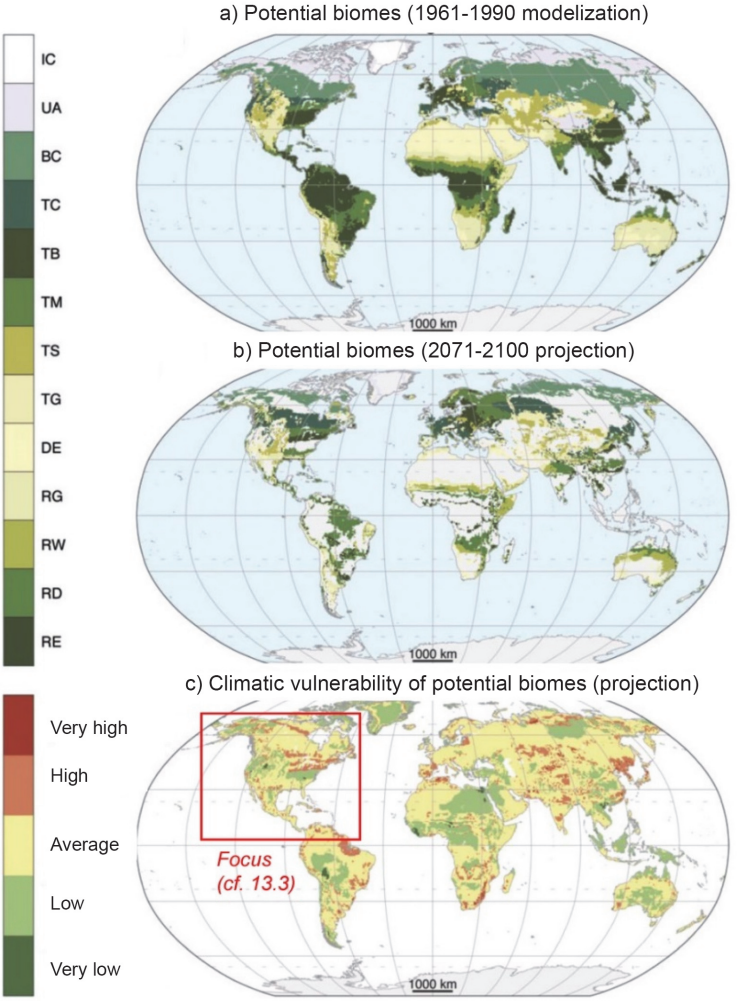

Figure 13.4. *Biome modeling*

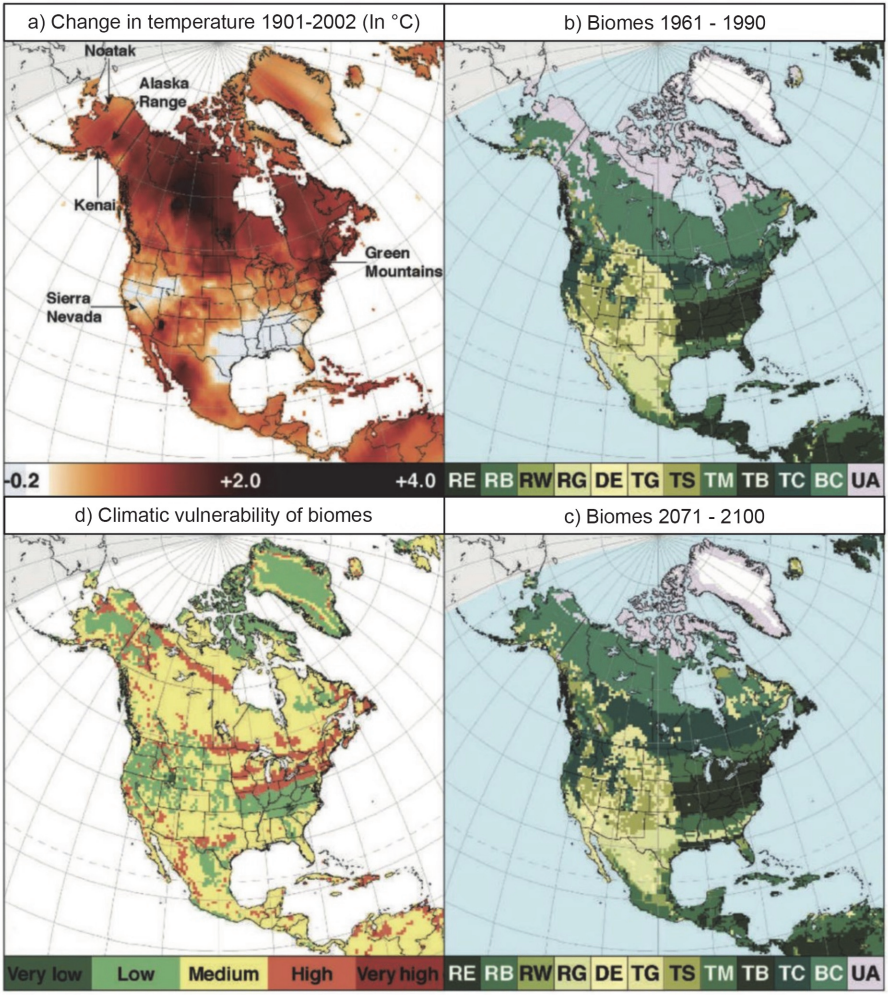

Figure 13.5. *Changes in assigned biomes to climate change in the United States*

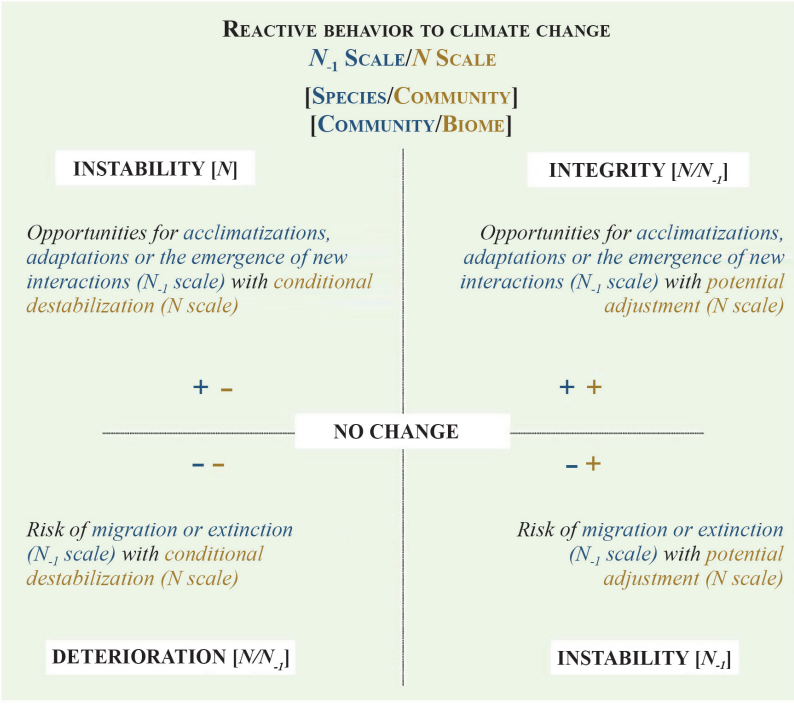

Figure 13.6. *Changes in biomes attributed to climate change (source: Gramond 2019)*

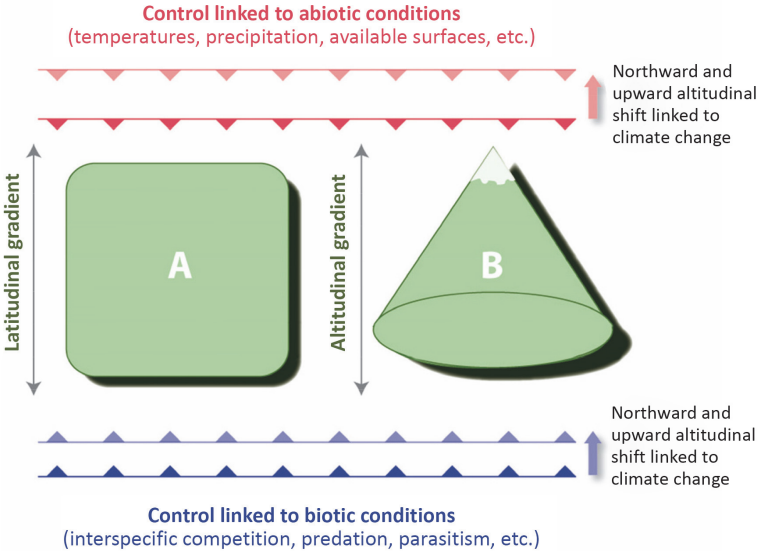

Figure 14.1. *The latitudinal (A) and altitudinal (B) limits of the birds' ranges are mainly controlled by abiotic factors (in red) at high latitudes (A) and altitudes (B), whereas the limits at low latitudes (A) and altitudes (B) are primarily controlled by biotic factors (in violet) (source: design and production, Laurent Godet)*

Figure 14.2. *The Royal Sunbird (*Cinnyris regius*, bottom), endemic to the Albertine Rift, and its biotope (top), here the Nyungwe montane rainforest in the south of Rwanda, are under serious threat from climate change (source: © Laurent Godet, October 2018, Nyungwe National Park, Rwanda).*

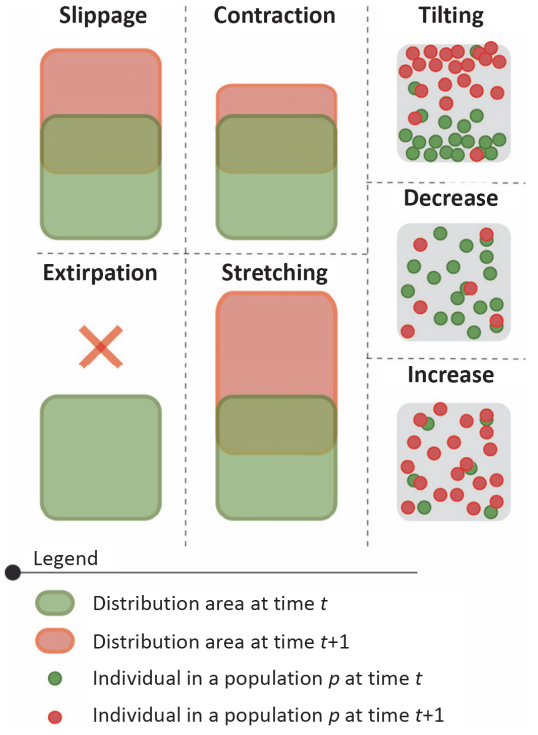

Figure 14.3. *Different patterns of change in species distribution as a consequence of climate change (source: design and production: Laurent Godet)*